

FRONT MATTER

Title

Long Title:

DeepForest: Sensing Into Self-Occluding Volumes of Vegetation With Aerial Imaging

Short Title:

DeepForest

Authors

Mohamed Youssef,¹ Jian Peng², and Oliver Bimber^{1*}

Affiliations

¹Johannes Kepler University Linz, Altenberger Straße 69, 4040 Linz, Austria.

²UFZ - Helmholtz Centre for Environmental Research, Permoserstraße 15, 04318 Leipzig, Germany.

*Corresponding Author: oliver.bimber@jku.at.

Abstract

Access to below-canopy volumetric vegetation data is crucial for understanding ecosystem dynamics. We address the long-standing limitation of remote sensing to penetrate deep into dense canopy layers. LiDAR and radar are currently considered the primary options for measuring 3D vegetation structures, while cameras can only extract the reflectance and depth of top layers. Using conventional, high-resolution aerial images, our approach allows sensing deep into self-occluding vegetation volumes, such as forests. It is similar in spirit to the imaging process of wide-field microscopy, but can handle much larger scales and strong occlusion. We scan focal stacks by synthetic-aperture imaging with drones and reduce out-of-focus signal contributions using pre-trained 3D convolutional neural networks. The resulting volumetric reflectance stacks contain low-frequency representations of the vegetation volume. Combining multiple reflectance stacks from various spectral channels provides insights into plant health, growth, and environmental conditions throughout the entire vegetation volume.

Teaser

Sensing below-canopy vegetation data to understand ecosystem dynamics is possible with conventional aerial imaging.

Introduction

Multi- and hyperspectral sensing are powerful techniques for observing vegetation, such as forests, that offer detailed insights into plant health, growth, and environmental conditions (1-11, 69-71). They play crucial roles in monitoring and understanding the impacts of climate change on ecosystems. Today, various remote sensors, such as cameras, radar, and Light Detection and Ranging (LiDAR) (1-4, 12-14), are used in combination with various platforms, such as satellites, airplanes and drones, or with ground-mounted and mobile field instruments. While radar, in particular synthetic-aperture radar (SAR), provides depth at lower spatial resolution than LiDAR but does not support multi-spectral measurement, it can be used to estimate structural parameters of vegetation or surfaces (15-18) and to derive specific radar vegetation indices (19,20). LiDAR (like radar) is an active sensor that does not rely on sunlight and instantly provides additional depth information in the form of point clouds from a single view, while point-cloud registration and filtering (12-14) must be carried out to merge overlapping scans taken from multiple views. Compared to LiDAR, cameras typically provide higher spatial resolution and wider spectral range coverage in near real time, are less complex and costly, weigh less and consume less power. Further, they reached technological maturity decades ago. Acquiring depth from camera recordings requires multi-view imaging and computer vision post-processing, such as photogrammetry.

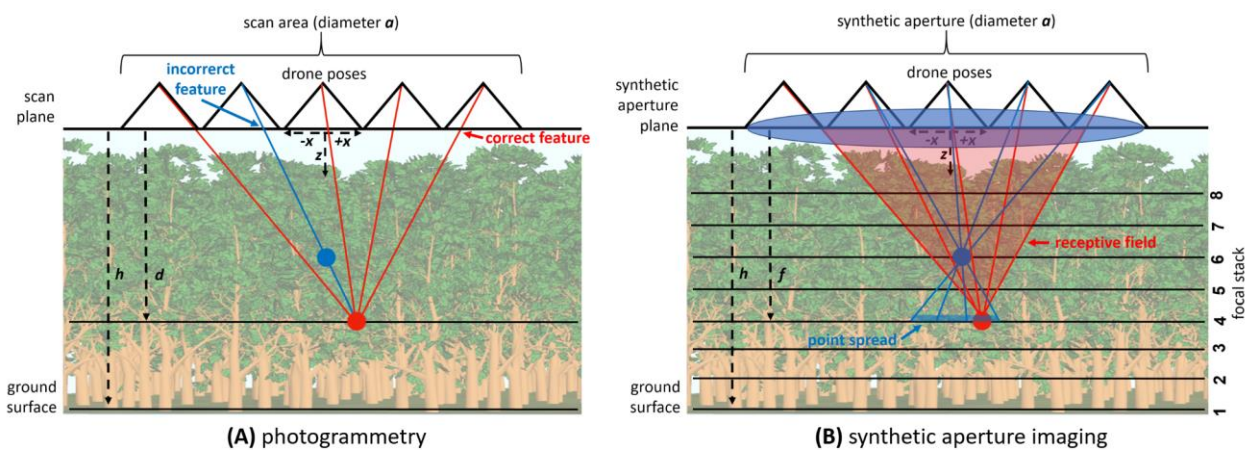


Fig. 1. Photogrammetry vs. synthetic-aperture imaging in the presence of partial occlusion. Dense forest vegetation captured with multiple aerial images at altitude h within sampling area a . The reconstruction of a scene point (red) at distance $d=f$ (depth=focal distance) is occluded in partial views by another scene point (blue). In photogrammetry (A), incorrectly matched features lead to reconstruction errors. In synthetic-aperture imaging (B), the point-spread signal of out-of-focus occluders in the receptive field leads to reconstruction errors of in-focus points at focal distance f .

Photogrammetric approaches, such as structure-from-motion and multi-view stereo (39-41), usually solve scene reconstruction by matching features in a large number of overlapping perspective images, and by finding estimates for camera poses and scene depth through optimization. Reconstructing deep vegetation layers and recovering correct reflectance values throughout all depth layers, however, is difficult to achieve with this. In photogrammetry (cf. Fig. 1A), deciding exactly which scene points appear unoccluded in which perspective image is not possible, and therefore best guesses are used, such as average values of all matched image features that contributed to a point's depth

estimation. If matched image features map to occluders, value estimation of photogrammetric stereo is error-prone. Furthermore, in the case of too few consistent feature matches, scene points are not reconstructed at all. This becomes even more problematic if inconsistent reconstruction from multiple spectral channels must be combined for vegetation-index estimation. The final outcomes are somewhat sparse reconstructions of the unoccluded top vegetation layer.

Our approach allows deeper sensing into self-occluding vegetation volumes using conventional aerial imaging, which brings with it the advantages of camera sensors, such as their lower complexity, cost, weight, and power consumption, as well as their significantly high spatial resolution and speed. We employ synthetic-aperture sensing, a signal-processing principle applied in fields such as radar (21-23, 15-20), interferometric microscopy (24), sonar (25), ultrasound (26-27), LiDAR (28-29), optical imaging (30-31), and radio telescopes (32-33). Synthetic-aperture imaging approaches (i.e., synthetic-aperture sensing applied to optical signals), such as Airborne Optical Sectioning (42-59), convert multi-view recordings (e.g., aerial images recorded by drones within a synthetic-aperture sampling area above forest) to a focal-stack representation (cf. Fig. 1B). A focal stack is an image stack that views the underlying environment from a constant overhead perspective, but at various optical focal distances in the viewing direction – similar to the focal-stack data set of a specimen captured by a wide-field microscope. In microscopy, for instance, focal stacks of semi-transparent specimens undergo 3D deconvolution (34-38) to remove out-of-focus contributions while depth-from-defocus (60-63) can be applied to focal stacks of opaque but unoccluded surfaces. However, in the presence of strong occlusion, as in our case, neither deconvolution nor depth-from-defocus is effectively feasible. Here, focal stack values of in-focus points contain contributions of the out-of-focus signal spread from opaque and non-transmissive occluders that are located within the corresponding three-dimensional receptive field defined by the synthetic aperture.

In this article, we present a novel approach to recovering the reflectance values at every point inside focal stacks of vegetation volumes. As illustrated in Fig. 2, we use drones to record multispectral images over multiple views within a synthetic-aperture sampling area above forest and compute a focal stack from these aerial images. Inspired by deconvolution in microscopy, we then correct the reflectance values of each point inside the focal stack with pre-trained three-dimensional convolutional neural networks (3D CNNs). The 3D CNNs were trained on focal stacks of simulated three-dimensional procedural forest environments to learn how to correct reflectance errors caused by out-of-focus signals of opaque occluders. The resulting volumetric representation (hereafter referred to as *reflectance stack*) provides low-frequency, but widely corrected, reflectance values. Reflectance stacks of multiple spectral channels can then be combined to a *vegetation-index stack*, which offers insights into plant health, growth, and environmental conditions throughout the entire vegetation volume, including its deep layers.

Our first finding is that focal stacks contain sufficient redundant information so that receptive fields with extremely low resolutions can be sampled. This leads to neural network architectures with a manageable number of parameters to be trained, and consequently to feasible computational and memory requirements. Our second finding is that, after correction, we can indeed recover reflectance information of deep vegetation layers that cannot be recovered by conventional image-based depth reconstruction, such as photogrammetry. Recovery of such information in multi- and hyperspectral channels can then be used to approximate vegetation indices of entire vegetation volumes. Our

approach is immediately applicable using established sensing platforms, such as drones or manned aircraft equipped with multispectral cameras. We present simulated results that allow comparison with ground-truth data, and results of real measurements acquired in the course of a first field experiment.

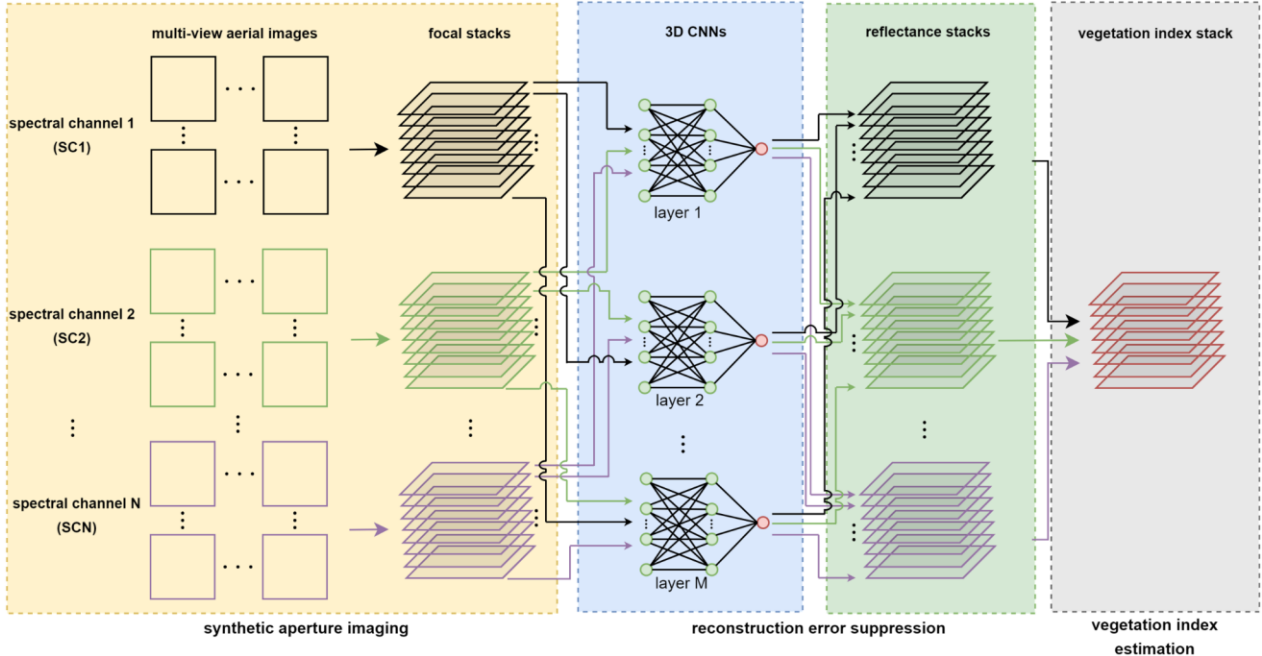


Fig. 2. Reconstruction architecture. Multi-view multispectral (SC=spectral channel) aerial images are converted into multispectral *focal stacks* by synthetic-aperture imaging. Out-of-focus errors in reflectance values of the focal stacks are suppressed using 3D convolutional neural networks (CNNs) that are pre-trained individually for each focal-stack layer, which yields multispectral *reflectance stacks*. The reflectance stacks are finally combined to a volumetric *vegetation-index stack*.

Results

Here, we describe the three main steps of our reconstruction architecture as illustrated in Fig. 2: *synthetic-aperture imaging*, *reconstruction-error suppression*, and *vegetation-index estimation*. We present quantitative results for simulations that provide ground truths, and visual results for simulations and a field experiment.

Synthetic-Aperture Imaging

Synthetic-aperture imaging techniques, such as Airborne Optical Sectioning (AOS) (42-59), exploit the parallax created when viewing partially occluded scenes from multiple aerial viewpoints. In Fig. 1B, as a drone flies at altitude h over an area of diameter a that represents a synthetic aperture (SA), it captures numerous images from various angles, each of which provides a unique line of sight through gaps between occluding obstacles, such as tree canopies and below-canopy layers. These images are then computationally combined by first registering them with respect to a selected synthetic focal plane at distance f (i.e., all aerial images are projected from their recording poses onto this focal plane) and then by integrating and normalizing (i.e., averaging) overlapping pixels. As in the case of conventional wide-aperture optics, the result is a shallow depth-of-field integral image that suppresses signals of out-of-focus occluders that are not located in the focal plane, while amplifying the image signals of in-focus points located in the focal plane. Because in-focus points remain at consistent positions across multiple projected views while random occluders appear in different positions, AOS can suppress effectively the occluding elements by spreading their blur signal widely over the entire integral image while enhancing the visibility of focussed features whose signals appear persistently in the same spot. After recording all views within the SA, an entire focal stack can be reconstructed by computing individual integral images for focal planes at selected focal distances f . Implementation details and source code can be found in previous work (42) and in the *Supplementary Materials*. Fig. 3 illustrates such a focal stack over 30 m x 30 m real and simulated forest plots.

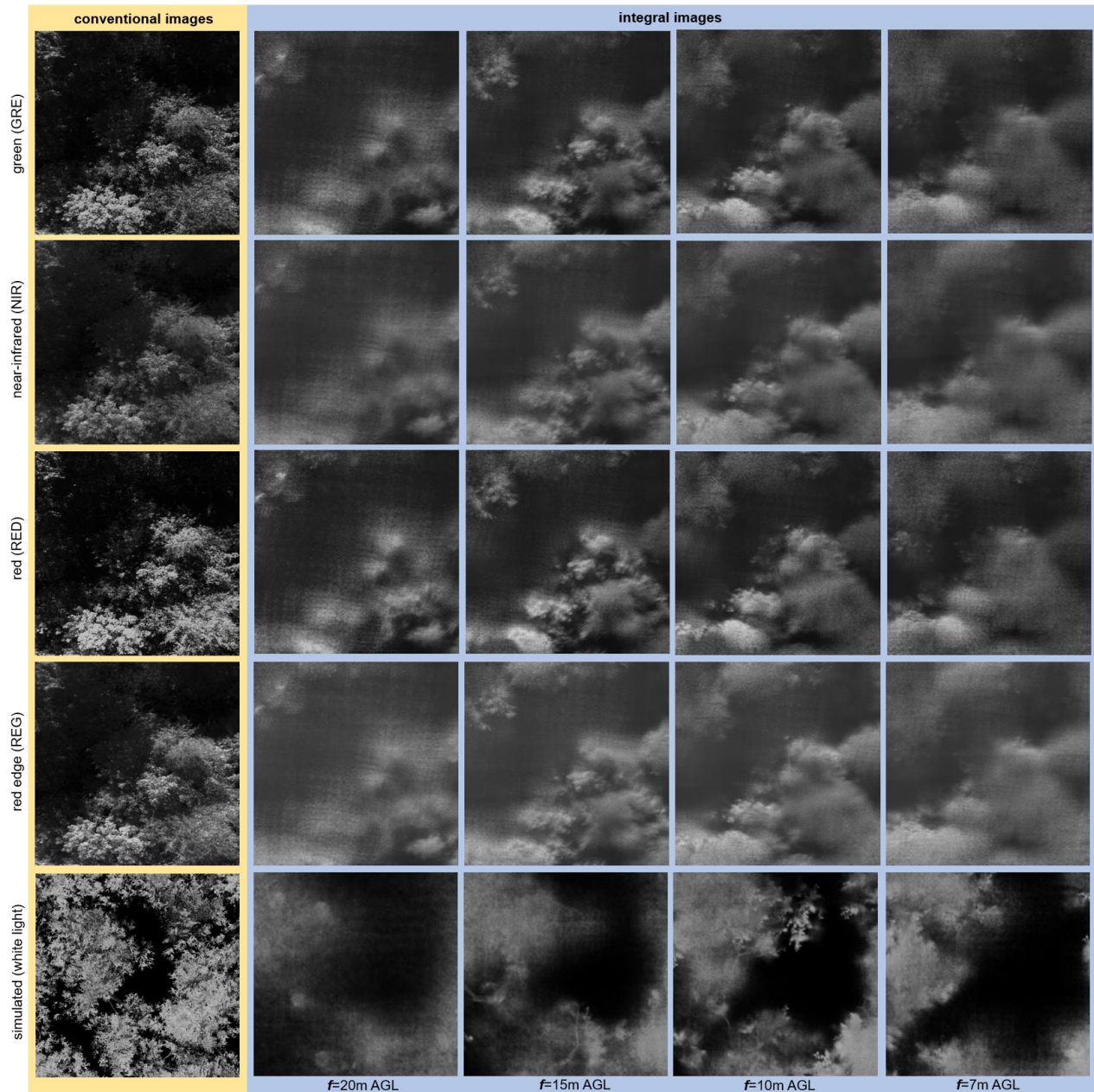


Fig. 3. Synthetic-aperture imaging. Multiple spectral bands (green, near-infrared, red, and red edge) captured at an altitude of 35 m above ground level (AGL) of a 30 m x 30 m mixed forest plot (top 4 rows). White-light procedural forest simulation under the same sampling conditions (bottom row). Conventional narrow-aperture camera images (left) and wide-aperture integral images (right) resulting from synthetic-aperture imaging (SA: $a=24$ m x 24 m, $h=35$ m AGL, 9x9 equidistant samples) when computationally focussing at different layers ($f=20$ m, 15 m, 10 m, 5m AGL). See *Supplementary Movies S1* and *S2* for animated versions of these results. The datasets are provided in the *Supplementary Materials*.

In principle, synthetic-aperture imaging is similar to the imaging process in wide-field microscopy, but the image signal of each layer in the focal stack is sampled and integrated computationally and discretely over the SA rather than being integrated optically and

continuously over the aperture of a lens. A simple mathematical approximation of this signaling process can be formalized with (cf. Fig. 1B):

$$V'(x, y, f) = \int_{x=-a/2}^{+a/2} \int_{y=-a/2}^{+a/2} \int_{z=f}^h V(x, y, z) \frac{1}{1 + \left(\frac{a}{f}|f-z|\right)^2}, \quad (1)$$

where $V'(x, y, f)$ is the integrated signal of a point at lateral position x, y in the focal plane at distance f , $V(x, y, z)$ the original signal of any point in the occlusion volume at lateral position x, y and axial distance z , a is the diameter of the synthetic aperture, h the distance between the synthetic-aperture plane and the forest ground, and a/f the f-number of the synthetic aperture.

Note that in the case of no occlusion (i.e., the defocussed signal spread of each point in V effects all other points in V that are located within the integrated receptive field, which depends on a and f) and assuming shift-invariance in x and y at f , the above formulation represents 3D convolution. A means of recovering V from V' is 3D deconvolution, as applied in wide-field microscopy for semi-transparent specimens, where the 3D point-spread function (PSF) of the imaging optics (that defines the optical receptive field) is assumed to be known, can be determined through calibration, or can be estimated blindly. However, deconvolution is ill-posed and not practically feasible in the presence of occlusion. Furthermore, the receptive field (i.e., our equivalent to the point-spread function in microscopy) is not constant, and therefore the signal error in our focal stacks is not equivalent to shift-invariant 3D convolution, as explained in Eqn. 1. For these two reasons, classical 3D deconvolution cannot be applied. This calls for a new reconstruction approach that suppresses reflectance error caused by (i) out-of-focus occluders and (ii) the presence of shift-variant occlusion.

Reconstruction Error Suppression

To suppress reflectance errors in a focal stack, we train an individual 3D convolutional neural network (CNN) for each of its layers. If we consider such a focal stack as a resolution of $V_w \times V_h \times V_d$, as illustrated in Fig. 4, we train V_d different 3D CNNs, the inputs to which are sampled values of other points in the focal stack that lie within the receptive field of a point to be corrected (including the value of the point itself). The receptive field is similar to the PSF in microscopy. However, since we assume full opacity and no transparency, it covers only the sub-areas in all the layers above that are within the frustum that spans from the in-focus points to the outer extent of the SA (i.e., the synthetic-aperture area in which the multi-view aerial images have been recorded). If the SA has a rectangular shape (as in our case, since we sampled it in a regular grid of, for example, 9x9 equidistant drone poses within a 24 m x 24 m area at an altitude of 35 m AGL), the receptive field has the shape of a (usually asymmetric) inverted pyramid. The number of layer fragments V_d' and their spatial resolution (max. $V_w' \times V_h'$) vary depending on the position of the corresponding in-focus point that needs to be corrected.

Full-resolution receptive fields as inputs would require excessive processing for data generation and huge sets of network parameters for training and inference. Therefore, we downsample them to much smaller sizes of $P_w \times P_h$ spatial resolution and P_d layers, where $P_w \ll V_w'$, $P_h \ll V_h'$, $P_d \ll V_d'$. Note that lateral downsampling (reducing the resolution of layer fragments) is achieved by averaging, while axial downsampling (reducing the number of layers) is achieved by nearest-neighbor subsampling (i.e., in-

between layers are ignored).

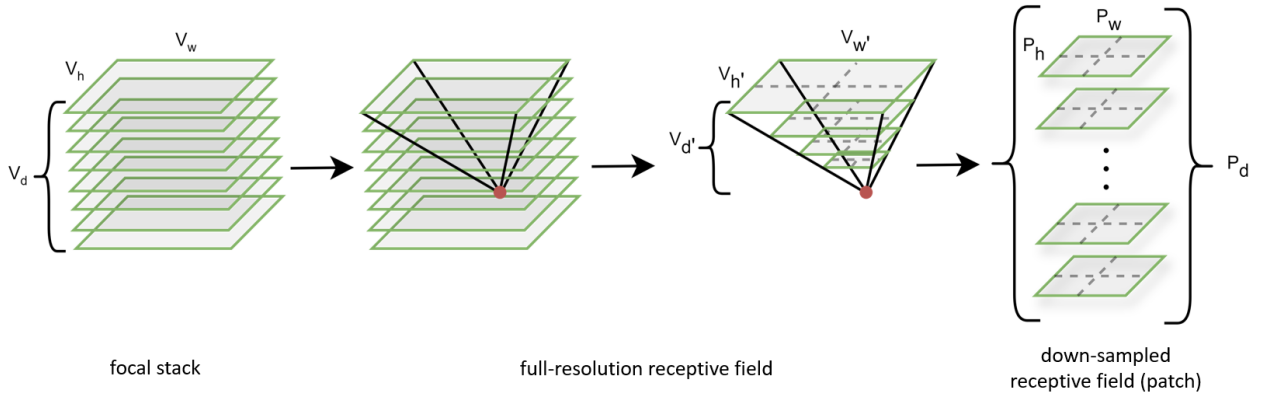


Fig. 4. Sampling the receptive field. The receptive field includes all out-of-focus points in a focal stack that add blur signal errors to in-focus points (red). It contains the sub-areas in all the layers above that are within the frustum that spans from the in-focus points to the outer extent of the synthetic aperture (which in our case is square). Sampling the receptive field as a low-resolution patch tensor reduces the number of parameters, network size, and processing effort significantly, and makes the training of 3D CNNs and their application for error suppression feasible within realistic lengths of time.

The resulting $P_w \times P_h \times P_d$ tensors (called *patches*) are the inputs to the layer-individual 3D CNNs, while the outputs are corrected reflectance values. Our 3D CNN model is illustrated in Fig. 5. It consists of eight 3D convolutional layers (conv 3D) with an increasing number (from 32 to 256) of activation slices. We apply the GELU (Gaussian Error Linear Units) activation function. A flatten layer maps the responses of the last convolution layer to a fully connected network with 128 perceptrons in its first layer, 64 perceptrons in its second layer, and one perceptron in its last layer. For each convolutional layer, the network learns $3 \times 3 \times 3$ kernels – summing to 6,143,009 parameters (for $P_w \times P_h \times P_d = 2 \times 2 \times 20$, including the parameters in the fully connected layers). Since we train such a network for each layer individually, the total number of parameters amounts to $V_d \times 6,143,009$ (i.e., 2,703,923,960 for $V_d = 440$, for example).

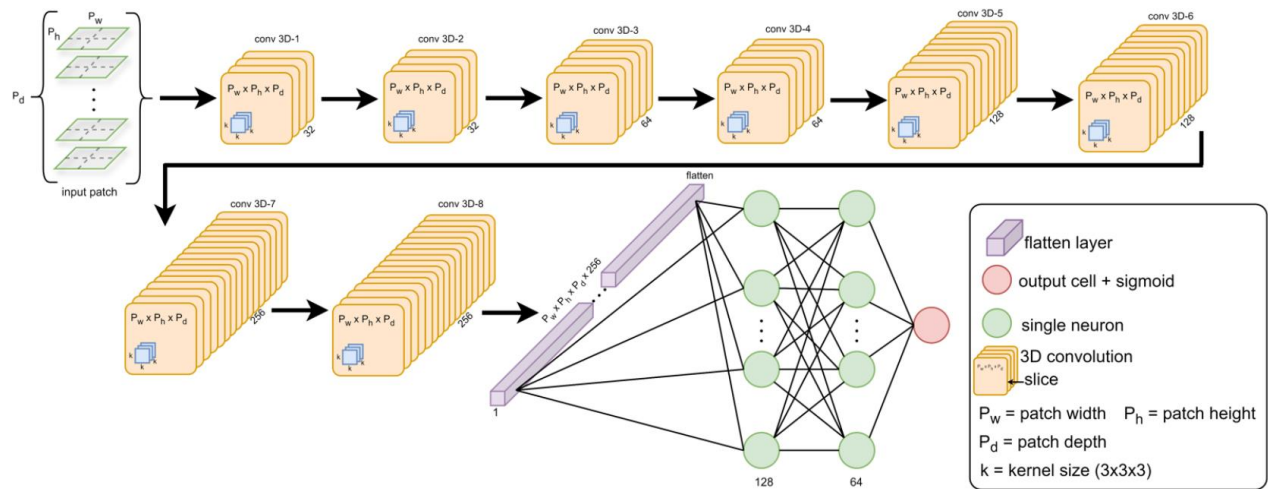


Fig. 5. 3D CNN model. Our 3D convolutional neural network model takes receptive field patches as input and outputs corrected reflectance values. It consists of eight convolutional layers of an increasing number of activation slices (32..256) with the same resolutions as the receptive field patches. Each activation slice is the output response of individually learned 3x3x3 kernels. A flatten layer maps the last convolutional layer to a 3-layer fully connected network (with 128/64/1 perceptrons).

We use the mean squared error (MSE) as a loss function to compare network results with ground-truth values, and Adam optimization (stochastic gradient-descent method based on adaptive estimation of first-order and second-order moments) for training the network. The training data which provides ground-truth values comes from simulated procedural forests with varying vegetation parameters, such as tree density (details provided in *Materials and Methods*). In our case, we used a total of 11,203,094 patches for training, 4,645,326 for validation, and 3,813,310 for testing. Note that since void points in 3D space do not have valid reflectance values, only patches that belong to non-void ground-truth points can be considered. As illustrated by the development of the training curves over multiple epochs (Fig. S1 of the *Supplementary Materials*), training does not converge to a minimum MSE if void points are included for training (assuming zero reflectance at these points).

Table 1 explores various patch-sampling options for layers at several heights f . It shows how model size and number of parameters exponentially increase with higher sampling resolutions. While MSE and RMSE (root-mean-square error) of the uncorrected reflectance values increase with deeper layers (due to a higher degree of occlusion), they remain fairly constant over all sampling resolutions and layers for the corrected reflectance values. Only undersampling (e.g., patch resolution: 2x2x3) prevents the model from converging. This finding suggests that focal stacks contain sufficient redundant information that receptive fields with extremely low resolutions can be sampled without sacrificing reconstruction quality. Thus, small models with feasible computational and memory requirements are sufficient. For all results described below, we therefore used a patch resolution of 2x2x20. Source code and pre-trained models are available in the *Supplementary Materials*.

f=20m AGL	Receptive Field Sampling ($P_w \times P_h \times P_d$)	Model Size (MB)	Number of Parameters	MSE (RMSE%) Corrected Uncorrected: 0.0022 (4.7%)	Uncorrected MSE / Corrected MSE
	2x2x3	15.20	3,914,785	-	-
	2x2x20	22.19	6,143,009	0.0014 (3.7%)	1.6
	2x2x40	36.95	8,764,449	0.0012 (3.5%)	1.8
	16x16x20	765.96	171,293,729	0.0016 (4.0%)	1.4
	16x16x40	1,518.48	339,065,889	0.0017 (4.1%)	1.3
f=15m AGL	Receptive Field Sampling ($P_w \times P_h \times P_d$)	Model Size (MB)	Number of Parameters	MSE (RMSE%) Corrected Uncorrected: 0.0035 (5.9%)	Uncorrected MSE / Corrected MSE
	2x2x3	15.20	3,914,785	-	-
	2x2x20	22.19	6,143,009	0.0012 (3.5%)	2.9
	2x2x40	36.95	8,764,449	0.0013 (3.6%)	2.7
	16x16x20	765.96	171,293,729	0.0013 (3.6%)	2.7
	16x16x40	1,518.48	339,065,889	0.0013 (3.6%)	2.7
f=10m AGL	Receptive Field Sampling ($P_w \times P_h \times P_d$)	Model Size (MB)	Number of Parameters	MSE (RMSE%) Corrected Uncorrected: 0.0044 (6.6%)	Uncorrected MSE / Corrected MSE
	2x2x3	15.20	3,914,785	-	-
	2x2x20	22.19	6,143,009	0.0014 (3.7%)	3.1
	2x2x40	36.95	8,764,449	0.0014 (3.7%)	3.1
	16x16x20	765.96	171,293,729	0.0013 (3.6%)	3.4
	16x16x40	1,518.48	339,065,889	0.0013 (3.6%)	3.4
f=7m AGL	Receptive Field Sampling ($P_w \times P_h \times P_d$)	Model Size (MB)	Number of Parameters	MSE (RMSE%) Corrected Uncorrected: 0.0060 (7.7%)	Uncorrected MSE / Corrected MSE
	2x2x3	15.20	3,914,785	-	-
	2x2x20	22.19	6,143,009	0.0014 (3.7%)	4.3
	2x2x40	36.95	8,764,449	0.0014 (3.7%)	4.3
	16x16x20	765.96	171,293,729	0.0014 (3.7%)	4.3
	16x16x40	1,518.48	339,065,889	0.0014 (3.7%)	4.3

Table 1. Receptive field sampling quality. Increasing patch resolution quickly leads to very large models (size in megabytes (MB) and number of parameters to train for one layer only). The reflectance error in uncorrected focal stacks increases with increasing occlusion for deeper layers. The remaining error after correction is fairly constant throughout all layers and all sampling resolutions (except for undersampling, 2x2x3, where our model does not converge). We use the mean squared error (MSE) and the root-mean-square error in % (RMSE%) to compare values with the ground truth. Note that all data was normalized (0..1). The improvement factor (last column) increases with deeper layers.

Simulated Results

For a better visual comparison, Fig. 6 illustrates a sparse example of a simulated procedural forest plot (220 trees/ha, 30 m x 30 m size with the highest tree tops at 20 m AGL) before and after correction. We simulate white-light reflection. Selected focal-stack slices of this plot are shown in Fig. 3 (bottom row). Compared to the ground truth, reflectance values of the uncorrected focal stack are mainly incorrect due to the point-spread signal of out-of-focus occluders. We apply the correction to every point of the focal stack (in our example of size 440x440x440 voxels) – including the void points. As explained in *Reconstruction Error Suppression*, void points do not have reflectance values, and their correction can therefore not be learned. For these points our model approximates low (yet not necessarily zero) reflectance values. A depth estimation of the entire volume would allow filtering out these void points. Photometric reconstruction, however, provides only a sparse point cloud of the top vegetation layer. Due to occlusion and inaccurate feature matching, reconstructed reflectance values are error-prone (especially at depth discontinuities, where the reflectance values of neighboring points change abruptly).

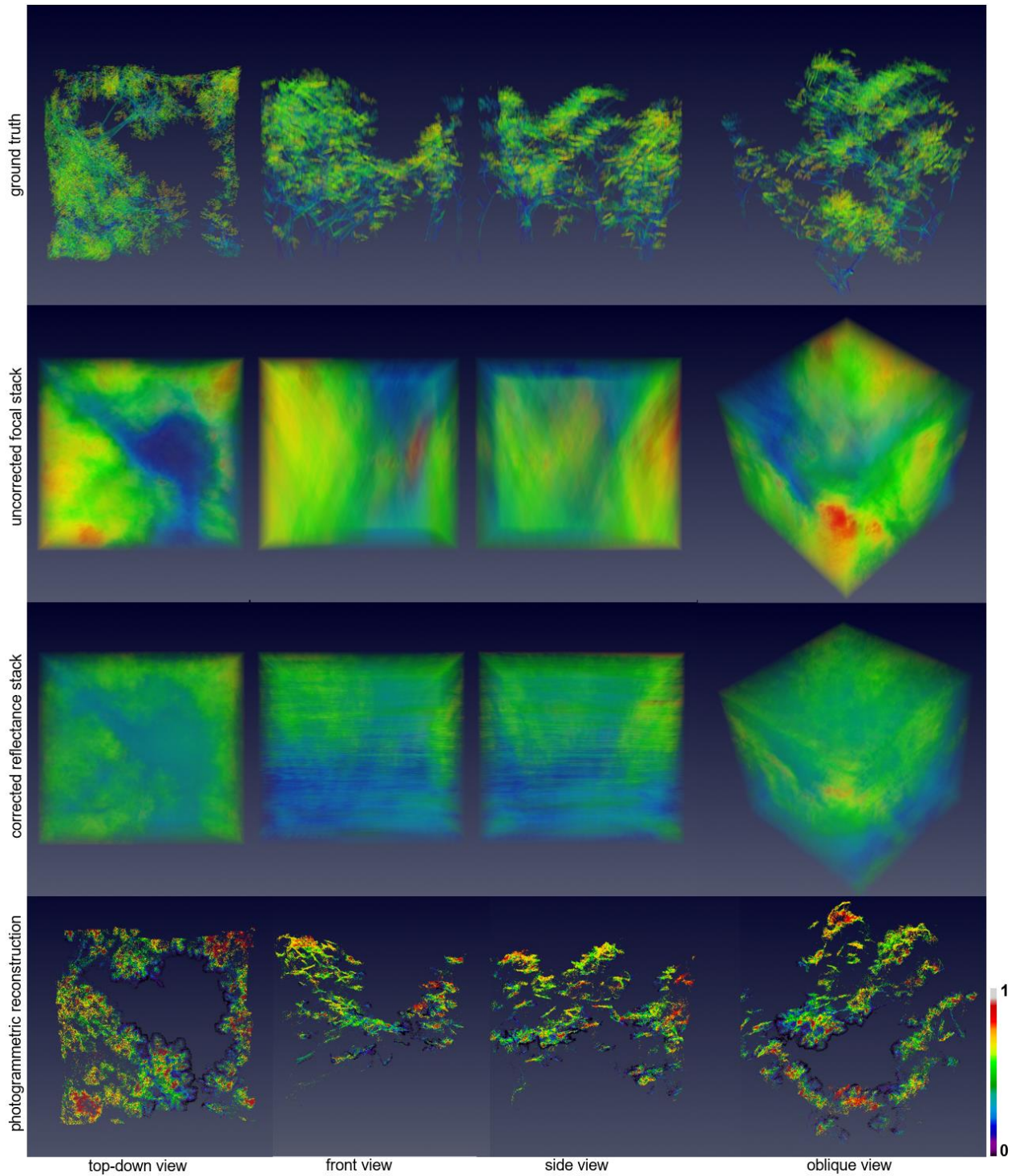


Fig. 6. Simulated reflectance correction. Different perspectives of a simulated sparse procedural forest plot (top row). Uncorrected focal stack (second row) and corrected reflectance stack (third row). Photometrically reconstructed (geometry and reflectance) point cloud (bottom row). Reflectance values are color-coded and within the same global range (0..1). Volumes are visualized with reduced opacity to display internal structures. Procedural forest simulation (details provided in *Materials and Methods*): 30 m x 30 m forest patch, highest tree crown at 20 m. Simulated aerial images: 440x440 px, captured over a 24x24 m SA (3 m sampling distance) at an altitude of 35 m AGL. Volume resolution: 440x440x440 voxels.

See *Supplementary Movie S1* for an animated version of these results. The datasets are provided in the *Supplementary Materials*.

Although the corrected reflectance stack does not contain spatial depth details because void points are not filtered, it reveals coarse geometric structures and approaches the ground-truth reflectance much better throughout all layers than the uncorrected focal stack (see *Supplementary Movie S1* and data provided in the *Supplementary Materials* for a better 3D impression of the reconstructed spatial structures). Detecting and assigning void points to zero opacity would recover all fine details at a resolution that is proportional to the camera resolution (see *Discussion* for potential options).

For the example shown in Fig. 6, Fig. 7A plots the MSE throughout all layers before and after correction (the four layers shown in Table 1 are part of it). Here we can see that the uncorrected error increases with the larger amount of accumulated occlusion in deeper layers (i.e., layers closer to the ground), while the error settles at a constant level after correction. This is possible because we train an individual 3D CNN for each depth layer and our models learn the depth-specific level of accumulated occlusion. Thus, our correction is less effective for higher layers with less occlusion ($\sim x2$ improvement) than for lower layers with more occlusion ($\sim x7$ improvement). While Figs. 6 and 7A present results for a sparse forest plot (220 trees/ha), Figures 7B,C show the MSE for various simulated forest densities (200 trees/ha ... 420 trees/ha). Although the MSE generally increases with a higher degree of occlusion, our correction leads to $\sim x6$ average improvements.

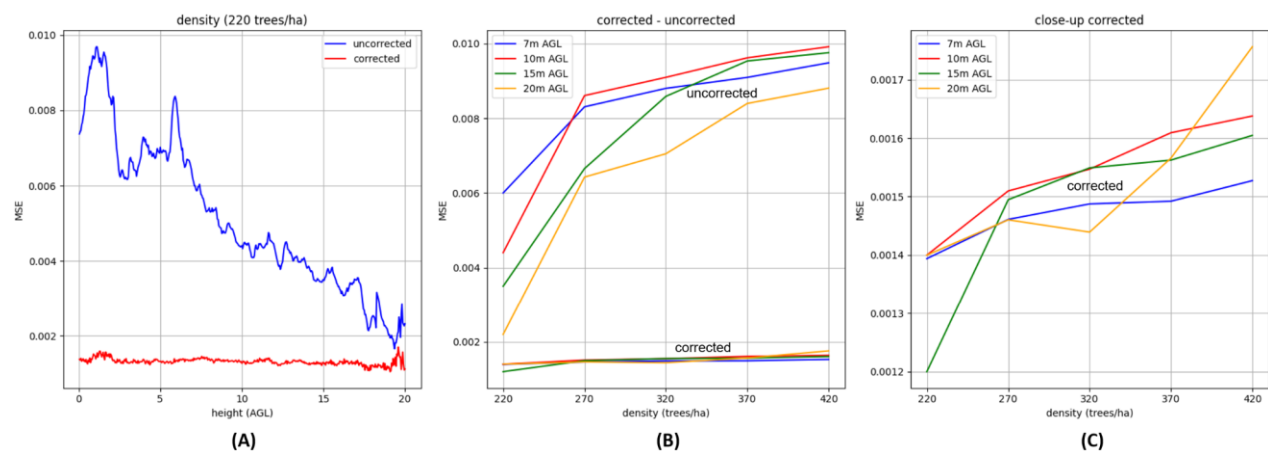


Fig. 7. Error for various vegetation layers and forest densities. (A) Development of the mean squared error (MSE) over various vegetation layers (0 m AGL = ground, 20 m AGL = highest tree top, simulated density: 220 trees/ha). The MSE of uncorrected reflectance values increases with lower layers due to more accumulated occlusion, while it remains constant throughout all layers after correction due to layer-individual correction models. (B) MSE for corrected and uncorrected reflectance values for four different layers (same as in Tab. 1) and for increasing simulated forest densities (200 trees/ha ... 420 trees/ha). While the MSE generally increases with increasing density, it is always significantly lower after correction. A close-up of the corrected cases in (B) is shown in (C).

Field Experiment with Vegetation-Index Estimation

Our field experiment took place at 1pm on October 25th, 2024, using a mixed broadleaf forest (birch, beech, oak; highest tree top at approx. 20 m AGL) near Linz in Upper Austria (GPS: 48.332773908818865, 14.33116356289388, see Fig. S2 of the *Supplementary Materials*). For scanning, we used a drone equipped with a four-band (red, green, near-infrared, red edge) multi-spectral camera (see *Materials and Methods* and Fig. S3 of the *Supplementary Materials*). As in our simulations, we scanned a 24 m x 24 m synthetic aperture at an altitude of 35 m AGL and a sampling distance of 3 m, covering a 30 m x 30 m plot on the ground. The drone flew automatically along a predefined GPS waypoint path, and the multispectral camera was triggered at intervals of 3 m flight distance. The scan flight took 18 minutes, including take-off and landing. The additional high-resolution RGB channel of the multispectral camera was used for precise pose estimation, and the multispectral images were undistorted, registered and radiometrically corrected (see *Materials and Methods*).

Since the sensor response of physical cameras most likely differs from that of the virtual camera used to generate the training data, we used sensor-mapping to support real cameras without the need to retrain our models (cf. Fig. 8A). For each spectral channel, we photogrammetrically reconstructed the topmost vegetation layer (see *Materials and Methods*) and mapped the resulting point cloud into the corresponding corrected reflectance stack. Since these points are unoccluded, their reflectance values should match the reflectance of the unoccluded points visible in the original camera images. We approximate this by matching their reflectance statistics and by correcting the reflectance stacks:

$$R' = \sigma_C(R - \mu_R) / \sigma_R + \mu_C, \quad (2)$$

where μ_C, σ_C are the reflectance mean and standard deviation of the center perspective camera image (i.e., the image captured at the synthetic aperture center), μ_R, σ_R are the reflectance mean and standard deviation of corrected reflectance stack values that are mapped to the reconstructed top vegetation layer point cloud within the same field of view as covered by the center perspective camera image, R are the corrected reflectance stack values before sensor-mapping and R' are the corrected reflectance stack values after sensor mapping. Figure 8 illustrates reflectance correction and sensor-mapping results of our field experiment for the near-infrared (NIR) and red (RED) channels.

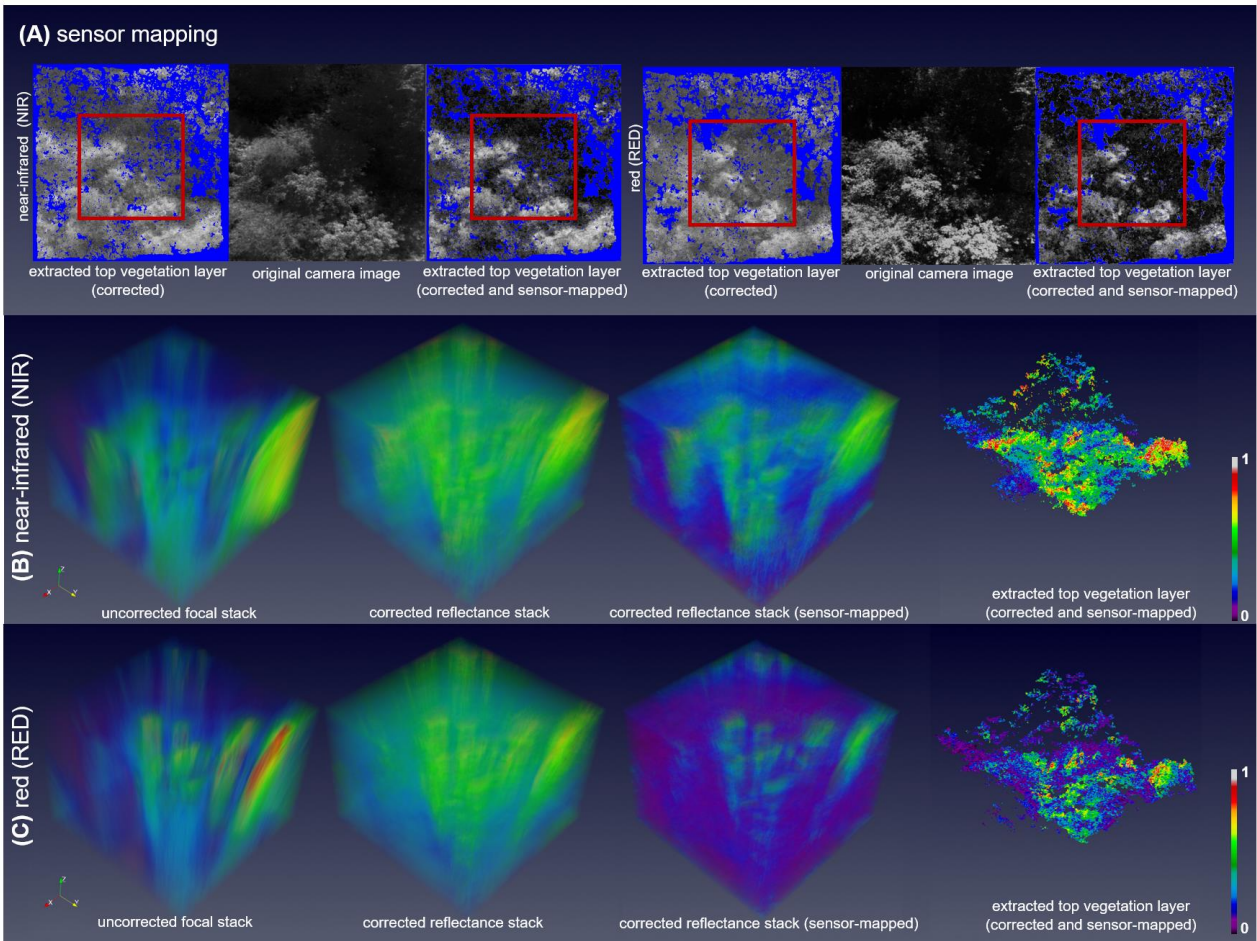


Fig. 8. Reflectance correction and sensor mapping. Sensor mapping by matching reflectance statistics of the top vegetation layer’s reconstructed point cloud with reflectance statistics of original camera image at the SA’s center (A). The red squares indicate the same field of view corresponding to that of the original camera image. Uncorrected focal stacks, corrected and sensor-mapped reflectance stacks, and extracted top vegetation-layer point clouds of NIR (B) and RED (C) channels. Reflectance values are color-coded and within the same global range (0..1). Volumes are visualized with reduced opacity to display internal structures. See *Supplementary Movie S2* for an animated version of these results. The datasets are provided in the *Supplementary Materials*.

We chose the frequently used *normalized difference vegetation index* (NDVI) (65) to demonstrate the estimation of a vegetation-index stack from the corrected reflectance stacks:

$$NDVI = (NIR - RED)/(NIR + RED), \quad (3)$$

where *NIR* and *RED* are values of corresponding voxels in the corrected and sensor-mapped near-infrared and red reflectance stacks, and *NDVI* is the resulting vegetation-index stack.

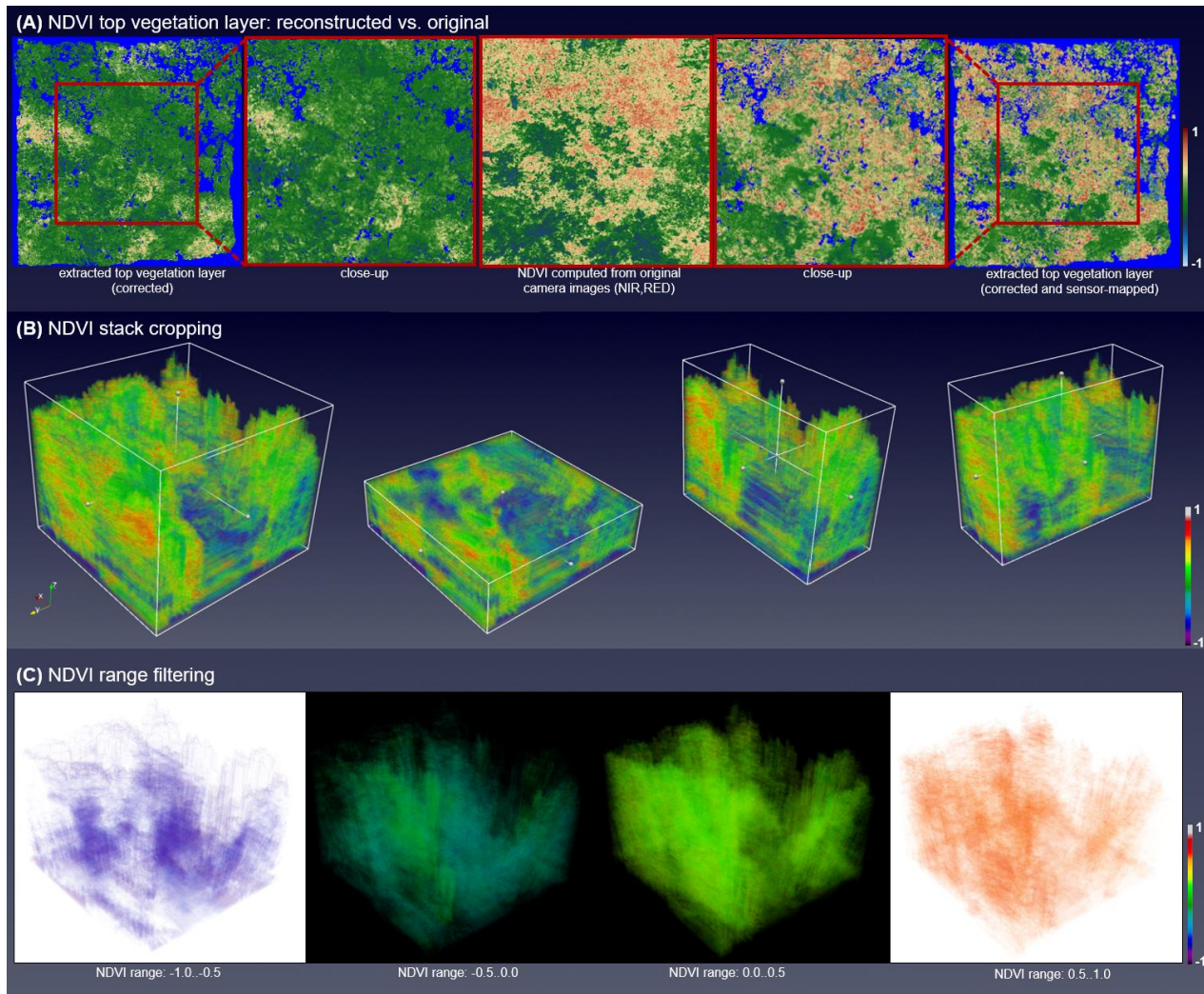


Fig. 9. NDVI stack. NDVI stack values determined from extracted top vegetation-layer point cloud (result of merging the photogrammetric reconstructions of the NIR and RED channels) with and without sensor mapping of the two spectral channels vs. NDVI image computed from original NIR and RED camera images (A). The red squares indicate the same field of view corresponding to that of the original camera image. The blue pixels represent points that could not be reconstructed with photogrammetry. NDVI stack cropping examples along all three axes (B). Filtering of four different NDVI ranges where only points within the corresponding range are displayed (C). Reflectance values are color-coded and within the same global range (-1..1). Note that in (A) we employed a color map commonly used for NDVI images, but in (B,C) we employed the color map used for volumes throughout this article, as this better highlights even small value variations in volumetric datasets. Volumes are visualized with reduced opacity to display internal structures. See *Supplementary Movie S3* for an animated version of these results. The datasets are provided in the *Supplementary Materials*.

Figure 9A illustrates results with and without sensor mapping applied to the corrected reflectance stacks before computing the NDVI stack. Unlike for the simulated data, we have no ground-truth reflectance values for our real measurements. We can, however, compare the NDVI values computed from the original NIR and RED camera images with the extracted top vegetation layer of the corresponding field of view from our NDVI stack

(Fig. 9A). Here, we achieved an overall MSE of 0.05 (RMSE% of 11.8%) with sensor mapping (MSE=0.2, RMSE%=22.4% without sensor mapping).

Figures 9B and 9C demonstrate further volume visualization options that are possible with our NDVI stack, such as cropping and range filtering. In both cases, we removed values of void points in the NDVI stack that were above the top vegetation layer point cloud (result of merging photogrammetric reconstructions of all spectral channels – here NIR and RED). In the case that no point was reconstructed for a particular x,y coordinate in the stack volume (i.e., no depth value in the axial z direction existed for a lateral coordinate), we applied nearest-neighbor interpolation to the point cloud's depth values. Note that low NDVI values indicate void areas and that low reflectance values generally lead to a low signal-to-noise ratio of NDVI values. By considering only NDVI values ≥ 0.33 , for example, we estimated the amount of moderately healthy to very healthy biomass in our NDVI stack to be 32.75% (which is equivalent to $3.793 \text{ m}^3/11.583 \text{ m}^3$). Note that the total below-canopy volume of 11.583 m^3 also contains void regions, non-green vegetation (e.g., soil and woody biomass, such as branches and trunks), and regions without sufficient sunlight reflection.

Discussion

Access to below-canopy volumetric vegetation data is crucial for understanding ecosystem dynamics, such as understory vegetation health, carbon sequestration, habitat structure, fuel load, and biodiversity (66-68). We have addressed a long-standing deficiency in remote sensing techniques, namely the inability to penetrate deep into dense canopy layers. Our new method retrieves volumetric reflectance data of entire vegetation profiles, which enables the assessment of ecological processes at a range of canopy depths. For example, visualizing vegetation indices across layers could help to monitor regeneration dynamics after disturbances such as deforestation or wildfires. The vegetation-index stacks could also reveal stress signals, such as droughts and pest outbreaks, that are not visible at the canopy levels, but are critical for forest ecosystem management. Further, volumetric information about biomass distribution may provide better estimates of the carbon storage potential of dense forests, where canopy-based data may underestimate carbon sequestration.

Our approach allows conventional aerial images to be used to sense deep into self-occluding vegetation volumes, such as forests. It is akin to the imaging process in wide-field microscopy, but is able to handle much larger scale and strong occlusion. We scan focal stacks by means of synthetic-aperture imaging and remove out-of-focus signal contributions using pre-trained 3D convolutional neural networks. We found that these focal stacks contain sufficient redundant information that receptive fields (our equivalent of point-spread functions in microscopy) with extremely low resolutions can be sampled (leading to manageable neural network architectures) and reflectance information of deep vegetation layers can be recovered. The volumetric reflectance stacks thus yielded contain low-frequency representations of the vegetation volume.

At the macroscopic scale, we assume that defocus depends only on imaging and geometry properties but is widely invariant to wavelength. Therefore, we can apply our (for white light trained) models to various spectral subbands. Combining multiple reflectance stacks from various spectral channels to vegetation-index stacks has the potential to provide insights into plant health, growth, and environmental conditions throughout the entire

vegetation volume, including its deep layers. Using classical vegetation indices, such as the NDVI, allows monitoring biomass, vegetation density and health in 3D volumes and volume segments.

Generalization

Our simulated results and field experiment were restricted to 30 m x 30 m plots scanned within a 24 m x 24 m synthetic aperture from 9x9 poses at an altitude of 35 m AGL. Our training data was also produced for these parameters. Consequently, our models learned to remove out-of-focus contributions caused by a synthetic aperture of corresponding (a/f) f-numbers (cf. Fig. 1B, Eqn. 1). Scanning larger regions, however, can simply be achieved by shifting the synthetic aperture and by reconstructing volume tiles (e.g., with the same synthetic-aperture parameters, a 300 m x 300 m plot can be reconstructed in 10x10 volume tiles). Since synthetic-aperture imaging relies strongly on the measurable parallax of close occluders (44), low flight altitudes are required. Compared to high-altitude flights, this leads to longer flight distances and scanning times to cover large areas. Scanning one-dimensional (i.e., along a continuous flight path) (50) instead of two-dimensional synthetic apertures, and using (one or more) high-speed fixed-wing drones or aircraft instead of multicopters, however, reduces the scanning time.

The procedural forest parameters (see *Materials and Methods*) used for our training data were chosen to approximate common European broadleaf forest vegetation. The occlusion statistics at various vegetation layers influence the point-spread signal of out-of-focus occluders in the receptive fields and thus the reconstruction error suppression. To consider the occlusion statistics of other types of vegetation, our models must be retrained with adapted procedural forest parameters. The same applies if the synthetic-aperture parameters are changed. Retraining, however, requires little computational effort (see *Limitations*). Source code and pre-trained models are available in the *Supplementary Materials*. Making larger training databases and pre-trained models available that cover diverse forest types and exploring more advanced forest simulators for generating such training databases will be part of our future work.

We employed a four-band spectral camera in our field experiments and used only the RED and NIR channels for NDVI computations (see *Materials and Methods*). To reduce processing times, raw images were downsampled to a resolution of 440x440 pixels, covering a 30 m x 30 m area on the ground. In theory, and considering 440 different focal distances over a height of 20 m, this is equivalent to a sampling resolution of approximately 6.8 cm x 6.8 cm x 4.5 cm per voxel. In practice, however, and as discussed in detail in (46), the lateral and axial resolutions of synthetic-aperture imaging depend not only on the image resolution, but also on the parameters of the synthetic aperture. In general, a higher spatial image resolution leads to a higher lateral (x,y) resolution of the image stacks. A wider synthetic aperture (i.e., area a in Fig. 1B) leads to a higher axial (z) resolution. A higher sampling resolution (i.e., number of single images captured) within the synthetic aperture reduces sampling artefacts in out-of-focus regions. Our approach scales to (i) higher image resolutions and more spectral channels, mainly at the cost of higher computational demands, and (ii) to more images captured over a wider SA, mainly at the cost of longer scanning times.

Limitations

The occlusion removal efficiency of synthetic-aperture imaging is limited by vegetation density. In theory and for uniform occlusion volumes (i.e., uniform distribution and

uniformly sized occluders), it has been shown (44) that visibility (V) relates to density (D) as $V=I-D^2$, and that a maximum visibility gain is achieved by synthetic-aperture imaging for $D=50\%$ densities. Below and above this threshold, it becomes less efficient – either because of too little occlusion (which renders its application less necessary) or because of too much occlusion (which makes occlusion removal less feasible). Too dense vegetation also prevents sunlight from penetrating into deeper layers, which causes low reflectance that might not be measurable with a limited camera dynamic range.

As discussed earlier, void points do not have reflectance values, and their correction can therefore not be learned. For these points our model approximates low (yet not necessarily zero) reflectance values that are noisy in the lateral and axial directions. This is why our reflectance stacks reveal only low-frequency vegetation features. Detecting and assigning void points to zero opacity would recover all fine details at a resolution proportional to the camera resolution. One possible solution would be to filter out these points by depth reconstruction. We already apply photogrammetric depth reconstruction to estimate the top vegetation layer and to filter out all void points above it. For occluded void regions below, however, we need to explore depth reconstruction techniques that are robust against self-occlusion. Depth-from-defocus (60-63) would in theory be ideal for focal stacks, but the state-of-the-art techniques are inefficient in the presence of strong occlusion. The potential of Neural Radiance Field (64) reconstructions will be explored in future. For sparse depth estimation, one might combine synthetic-aperture imaging with active scanning, such as LiDAR or radar. A second solution would be to consider a consistency regularization in our loss function that suppresses spatial noise during the training process. A third option would be post-filtering the noise in the reconstructed reflectance stacks (note that all results presented are raw and unfiltered). However, alpha-blending of volume visualization with reduced opacities has a similar effect.

The general limitations of vegetation indices are inherited. The NDVI, for instance, is sensitive to chlorophyll content but limited by atmospheric noise and saturation in high biomass areas (73). Alternatives, such as the *normalized difference red edge* (NDRE) index (69), which is sensitive to chlorophyll content in higher biomass areas, might be more suitable for dense vegetation volumes. A low signal-to-noise ratio of reflectance values also leads to a low signal-to-noise ratio of vegetation indices.

Our current implementation is not performance-optimized. On an INTEL Core i9-13900KF together with an NVIDIA GeForce RTX 4090, the computation of training data (including procedural forest generation, focal stack computation, and training data preparation) for one 30 m x 30 m simulated forest plot takes around 40 min, model training for one depth layer approx. 15 min, and reconstruction of one point in a reflectance stack approx. 15 ms. Our computations are highly parallelizable. Inference (of points and depth layers in reflectance stacks or vegetation-index stacks) is independent and could therefore be scaled efficiently to clusters. Furthermore, filtering out void points first and then applying reflectance correction only to non-void points would reduce the overall processing time. In addition to performance optimizations, more sophisticated sensor-mapping techniques that support non-linear sensor transfer functions need to be investigated.

Passive vs. Active Sensing

Passive multi- and hyperspectral camera sensors (5-11,70,71,73) have only been able to extract reflectance and depth of top vegetation layers. Active L-band (15) or P-band

(16,17) radar is able to penetrate deeper into vegetation volumes, but its spatial resolution is lower than that of LiDAR or cameras. It mainly supports structural estimation of surfaces and biomass, but not multi-spectral measurement. Active multi- and hyperspectral LiDAR sensors (1-4,72) can measure multiple returns of laser light reflected from various height levels, but scanning speed is traded off against sampling resolution. Up to now, LiDAR and radar have therefore been considered the primary technologies for measuring and modeling 3D forest structures. However, only multi- and hyperspectral LiDAR and cameras provide the spectral information necessary for vegetation health monitoring, as they capture data in specific wavelength bands relevant to plant-physiological processes. Although combinations of radar or LiDAR with multi- and hyperspectral cameras exist (1,13,14,74), conventional aerial imaging has not solved the problem of occlusion and captures predominantly only the topmost layers of vegetation. We have presented here an approach that enables existing passive and high-resolution camera systems to sense deeper into vegetation.

Active and passive approaches each have advantages and disadvantages: The main advantages of active LiDAR or radar sensors are their capability of directly estimating depth and independence of sunlight. However, sunlight and scattering and speckle of the laser illumination in dense vegetation lead to signal interference for LiDAR, while terrain effects (e.g., multi-scattering, varying surface slopes and incident angles, radar shadow, and layover effects) result in incorrect radar measurements. Dense occlusion, as in our case, is problematic for both LiDAR and radar. It can be overcome by measuring from multiple poses over a wider range (i.e., over a wider synthetic aperture) that provide locally unobstructed views, but scattering artefacts in dense vegetation may occur.

The main advantages of passive camera sensors are their lower complexity, cost, weight, and power consumption, and their significantly high spatial resolution and speed. It is easy to deploy our software approach on a wide range of existing drone platforms, including fast fixed-wing systems and drone swarms that can scan large areas in parallel. Even drone platforms with conventional RGB cameras can be supported in combination with vegetation indices that emphasize vegetation in the visible spectrum, such as the *visible atmospherically resistant index* (VARI) (75). Furthermore, our approach can directly be applied to thermal camera sensors to allow simultaneous assessment of water stress and thermal regulations within vegetation volumes. Measuring thermal radiation is not possible with active sensors, such as LiDAR or radar. Instead of top-down, above-canopy aerial imaging, bottom-up, under-canopy drone scans (76-78) together with computation of transmittance-based vegetation indices (79,80) can also be contemplated using our method.

There is also potential to advance ecological monitoring by integrating our passive approach with active remote-sensing technologies. While LiDAR provides depth information that helps to filter out void points below the canopy in our reflectance stacks, synthetic-aperture radar could complement our method by providing vegetation water content and canopy structure under cloudy and low-light conditions. The integration of multiple sensors enables comprehensive monitoring of vertical vegetation layers, which has significant implications for ecological research into dynamic ecosystems. In tropical rainforests, such as the Amazon rainforest, it could reveal the impacts of climate change and deforestation on understory biodiversity and carbon storage. In temperate forests, it could track seasonal changes in the NDVI to improve phenological models and thus

support sustainable forest management. For dryland vegetation, it could improve the understanding of efficient water use and drought resilience.

Materials and Methods

Procedural Forest Simulation

Our simulated environments were created with the procedural forest generation algorithm integrated within a GAZEBO-based drone simulator (https://github.com/bostelma/gazebo_sim, *Supplementary Code S1*). We computed RGB images at a resolution of 440x440 px, capturing aerial images across specified synthetic-aperture regions (24 m x 24 m in our examples) with customizable flight parameters (altitude of 35 m AGL and 3 m sampling distance in our examples). At the macroscopic scale, we assumed that defocus depends only on imaging and geometry properties but is largely invariant to wavelength. Thus, the RGB channels were averaged to simulate white-light reflectance values. All aerial images were captured using a virtual drone camera with a 50° field of view, configured for perspective projection and oriented perpendicular to the ground plane (nadir = downward-facing).

We configured the procedural trees with varying parameters to approximate European broadleaf forest: heights ranging from 5 to 20 m, trunk lengths between 4 and 8 m, trunk diameters of 20 to 50 cm, and leaf dimensions varying from 5 to 20 cm. Tree variety was achieved using a seeded random generator which controlled both the distribution and similarity patterns of the trees. The simulations maintained constant environmental conditions, including tree species composition, foliage characteristics, and seasonal settings. We simulated forest densities of 200-420 trees per hectare.

Pose Estimation and Photogrammetric Reconstruction

For photogrammetric reconstruction and pose estimation, we used the structure-from-motion and multi-view stereo framework COLMAP (39-41, <https://colmap.github.io/>) and resampled the resulting point cloud in a volumetric stack of the same resolution as our focal, reflectance, and vegetation-index stacks.

Focal Stack Computations

The result of synthetic-aperture imaging, be it simulated or physically recorded, is a grid of aerial images with corresponding poses. In our examples, this grid was 9x9 images (covering a 24 m x 24 m synthetic aperture at a 3 m sampling distance). To reduce computational complexity, we restricted images to a resolution of 440x440 px (captured images were cropped and downsampled to this resolution) and ensured that the field-of-views of simulated and real cameras matched. We used the Airborne Optical Section software (<https://github.com/JKU-ICG/AOS>) to compute focal stacks with predefined heights (from 0 m to 20 m AGL in our examples) and number of slices (440 in our examples) from the grid of input image and poses.

Training, Validation, and Inference

Our 3D CNN architecture was implemented in Python 3.11.7 with PyTorch 2.5.1 and CUDA 12.6 for GPU acceleration (see *Supplementary Code S2* for training and reconstruction source code and *Supplementary Data S1* for pre-trained models). It was trained, validated, and inferred on an INTEL Core i9-13900KF together with an NVIDIA GeForce RTX 4090.

Data Processing and Visualization

Uncorrected focal stacks, corrected reflectance stacks, and vegetation-index stacks were initially stored in single images (.png) per layer. We applied ImageJ (<https://imagej.net/>) to combine these single images into one image stack (.tif). We then embedded these image stacks and voxelized COLMAP point clouds (from photogrammetry or simulated ground-truth geometry) in multiple magnitude and opacity layers of the same file (.vti). Original COLMAP results (reconstructed geometry and reflectance) were stored as point clouds (.vtk). We used ParaView (<https://www.paraview.org>) for volume (.vti) and point-cloud (.vtk) rendering. See *Supplementary Materials* for a detailed description of all supplementary datasets.

Drone Platform for Field Experiment

For scanning real forest environments, we used a DJI Matrice 30T drone (<https://enterprise.dji.com/matrice-30>) equipped with an additional Parrot Sequoia+ multispectral camera (<https://www.parrot.com/en/support/documentation/sequoia>). See Fig. S3 of the *Supplementary Materials*. The camera simultaneously captures four bands: green (550 nm wavelength, 40 nm bandwidth), red (660 nm wavelength, 40 nm bandwidth), red edge (735 nm wavelength, 10 nm bandwidth) and near infrared (790 nm wavelength, 40 nm bandwidth) at a 1.2 megapixel resolution (1,280x960 px). In addition to the four monochrome sensors, it has a 16 megapixel (4,608x3,456 px) RGB sensor, a sunlight sensor to compensate for variations in environmental light conditions, and an integrated GPS/GNSS for position-based triggering. After triggering at desired sampling distances (3 m in our experiments), multispectral and RGB images are stored in 64GB internal memory and can be downloaded and processed after landing. The multispectral camera was attached to the bottom of the drone (nadir = downward-facing) while the sunlight sensor was attached to the drone's top (upwards-facing). Both camera and sunlight-sensor were powered by the drone's batteries via DJI's e-port. The total take-off weight with all components attached was below the legal limit of 3.7 kg. The camera was calibrated before flight (based on the manufacturer's guidelines), and all multispectral images recorded were undistorted, registered and radiometrically corrected using the Sequoia image processing tools (https://github.com/rasmusfenger/micasense_imageprocessing_sequoia).

References

1. R. Trouvé, R. Jiang, M. Fedrigo, M.D. White, S. Kasel, P.J. Baker, C.R. Nitschke, Combining Environmental, Multispectral, and LiDAR Data Improves Forest Type Classification: A Case Study on Mapping Cool Temperate Rainforests and Mixed Forests. *Remote Sens.* **15**, 60 (2023).
2. Y. Zhao, J. Im, Z. Zhen, Y. Zhao, Towards accurate individual tree parameters estimation in dense forest: optimized coarse-to-fine algorithms for registering UAV and terrestrial LiDAR data. *GIScience & Remote Sensing*, **60**, (2023).
3. Y. Jiao, D. Wang, X. Yao, S. Wang, T. Chi, Y. Meng, Forest Emissions Reduction Assessment Using Optical Satellite Imagery and Space LiDAR Fusion for Carbon Stock Estimation. *Remote Sens.* **15**(5), 1410 (2023).
4. M. Yan, Y. Xia, X. Yang, X. Wu, M. Yang, C. Wang, Y. Hou, D. Wang, Biomass Estimation of Subtropical Arboreal Forest at Single Tree Scale Based on Feature Fusion of Airborne LiDAR Data and Aerial Images. *Sustainability.* **15**(2), 1676 (2023).
5. N. Farmonov, K. Amankulova, J. Szatmári, A. Sharifi, D. Abbasi-Moghadam, S. M. Mirhoseini Nejad, L. Mucsi, Crop Type Classification by DESIS Hyperspectral Imagery

- and Machine Learning Algorithms. *IEEE Journal of Selected Topics in Applied Earth Observations and Remote Sensing*, **16**, 1576-1588 (2023).
6. S.-J. Hong, S. Park, A. Lee, S.-Y. Kim, E. Kim, C.-H. Lee, Ghiseok Kim, Nondestructive prediction of pepper seed viability using single and fusion information of hyperspectral and X-ray images. *Sensors and Actuators A: Physical*, **350**, 114151 (2023).
 7. Z. Lou, L. Quan, D. Sun, H. Li, F. Xia, Hyperspectral remote sensing to assess weed competitiveness in maize farmland ecosystems. *Science of The Total Environment*, **844**, 157071 (2022).
 8. B. Gao, L. Yu, L. Ren, Z. Zhan, Y. Luo, Early Detection of *Dendroctonus valens* Infestation at Tree Level with a Hyperspectral UAV Image. *Remote Sens*, **15**, 407 (2023).
 9. S. Fei, L. Li, Z. Han, Z. Chen, Y. Xiao, Combining novel feature selection strategy and hyperspectral vegetation indices to predict crop yield. *Plant Methods*, **18**, 119 (2022).
 10. S.-Y. Chen, M.-F. Chiu, X.-W. Zou, Real-time defect inspection of green coffee beans using NIR snapshot hyperspectral imaging. *Computers and Electronics in Agriculture* **197**, 106970 (2022).
 11. Y. Cao, P. Yuan, H. Xu, J. F. Martínez-Ortega, J. Feng, Z. Zhai, Detecting Asymptomatic Infections of Rice Bacterial Leaf Blight Using Hyperspectral Imaging and 3-Dimensional Convolutional Neural Network With Spectral Dilated Convolution. *Front. Plant Sci.*, **13**, (2022).
 12. N. Tsoulias, K. K. Saha, M. Zude-Sasse, In-situ fruit analysis by means of LiDAR 3D point cloud of normalized difference vegetation index (NDVI). *Computers and Electronics in Agriculture*, **205**, 107611 (2023).
 13. C. Míguez, C. Fernández, Evaluating the Combined Use of the NDVI and High-Density Lidar Data to Assess the Natural Regeneration of *P. pinaster* after a High-Severity Fire in NW Spain. *Remote Sens.*, **15**, 1634 (2023).
 14. C. J. Iheaturu, S. Hepner, J. L. Batchelor, G. A. Agonvonon, F. O. Akinyemi, V. R. Wingate, C. Ifejika Speranza, Integrating UAV LiDAR and multispectral data to assess forest status and map disturbance severity in a West African forest patch. *Ecological Informatics*, **84**, 102876 (2024).
 15. Z. Ye, J. Long, T. Zhang, B. Lin, H. Lin, L-Band Synthetic Aperture Radar and Its Application for Forest Parameter Estimation, 1972 to 2024: A Review. *Plants*, **13**, 2511 (2024).
 16. G. Sandberg, L. M. H. Ulander, J. Wallerman, J. E. S. Fransson, Measurements of Forest Biomass Change Using P-Band Synthetic Aperture Radar Backscatter. *In IEEE Geosci. Remote Sens.*, **52**, 6047-6061 (2014).
 17. Y. Xu, Z. Lu, R. Bürgmann, S. Hensley, E. Fielding, J. Kim, P-band SAR for ground deformation surveying: Advantages and challenges. *Remote Sens. Environ.*, **287**, 113474 (2023).
 18. M.A. Wulder, T. Hilker, J.C. White, N.C. Coops, J.G. Masek, D. Pflugmacher, Y. Crevier, Virtual constellations for global terrestrial monitoring. *Remote Sens. Environ.*, **170**, 62-76 (2015).
 19. X. Hu, L. Li, J. Huang, Y. Zeng, S. Zhang, Y. Su, Y. Hong, Z. Hong, Radar vegetation indices for monitoring surface vegetation: Developments, challenges, and trends. *Science of The Total Environment*, **945**, 173974 (2024).
 20. S. Kaasalainen, M. Holopainen, M. Karjalainen, M. Vastaranta, V. Kankare, K. Karila, B. Osmanoglu, Combining lidar and synthetic aperture radar data to estimate forest biomass: status and prospects. *Forests*, **6(1)**, 252-270 (2015).
 21. A. Moreira, P. Prats-Iraola, M. Younis, G. Krieger, I. Hajnsek, K. P. Papathanassiou, A tutorial on synthetic aperture radar. *IEEE Geosci. Remote Sens.* **1**, 6-43 (2013).

22. C. J. Li, H. Ling, Synthetic aperture radar imaging using a small consumer drone. *In 2015 IEEE International Symposium on Antennas and Propagation USNC/URSI National Radio Science Meeting*, Vancouver, BC, Canada, 685-686 (2015).
23. P.A. Rosen, S. Hensley, I.R. Joughin, F.K. Li, S.N. Madsen, E. Rodriguez, R.M. Goldstein, Synthetic aperture radar interferometry. *Proc. IEEE*, **88**, 333–382 (2000).
24. T.S. Ralston, D.L. Marks, P.S. Carney, S.A. Boppart, Interferometric synthetic aperture microscopy (ISAM). *Nat. Phys.* **3**, 965–1004 (2007).
25. M.P. Hayes, P.T. Gough, Synthetic aperture sonar: a review of current status. *IEEE J. Ocean. Eng.* **34**, 207–224 (2009).
26. J.A. Jensen, S.I. Nikolov, K.L. Gammelmark, M.H. Pedersen, Synthetic aperture ultrasound imaging. *Ultrasonics*. **44**, 5–15 (2006).
27. H.K. Zhang, A. Cheng, N. Bottenus, X. Guo, G.E. Trahey, E.M. Boctor, Synthetic tracked aperture ultrasound imaging: design, simulation, and experimental evaluation. *J. Med. Imaging*. **3**, 027001 (2016).
28. Z.W. Barber, J.R. Dahl, Synthetic aperture lidar imaging demonstrations and information at very low return levels. *Appl. Opt.* **53**, 5531–5537 (2014).
29. S. Turbide, L. Marchese, M. Terroux, A. Bergeron, Synthetic aperture lidar as a future tool for earth observation. *Proc. SPIE*. **10563**, 1115-1122 (2017).
30. T. Yang, W. Ma, S. Wang, J. Li, J. Yu, Y. Zhang, Kinect based real-time synthetic aperture imaging through occlusion. *Multimed. Tools Appl.* **75**, 6925–6943 (2016).
31. Z. Pei, Y. Li, M. Ma, J. Li, C. Leng, X. Zhang, Y. Zhang, Occluded-object 3D reconstruction using camera array synthetic aperture imaging. *Sensors* **19**, 607 (2019).
32. R. Levanda, A. Leshem, Synthetic aperture radio telescopes. *IEEE Signal Process. Mag.*, **27**, 14–29 (2010).
33. D. Dravins, T. Lagadec, P.D. Nuñez, Optical aperture synthesis with electronically connected telescopes. *Nat. Commun.* **6**, 6852 (2015).
34. D. Sage, D. Lauréne, S. Ferréol, F. Denis, S. Guillaume, S. Arne, G. Romain, V. Cédric, U. Michael, DeconvolutionLab2: An open-source software for deconvolution microscopy. *Methods*. **115**, 28-41 (2017).
35. J.G.McNally, T.Karpova, J.Cooper, J.A.Conchello, Three-dimensional imaging by deconvolution microscopy. *Methods*, **19(3)**, 373–385 (1999).
36. P.Sarder, A.Nehorai, Deconvolution methods for 3-D fluorescence microscopy images, *IEEE Signal Processing Mag.*, **23(3)**, 32–45 (2006).
37. B. Kim, T. Naemura, Blind depth-variant deconvolution of 3D data in wide-field fluorescence microscopy, *Sci. Rep.* **5**, 9894 (2015).
38. J. Ajdenbaum, E. Chouzenoux, C. Lefort, S. Martin, J. C. Pesquet, A novel variational approach for multiphoton microscopy image restoration: from PSF estimation to 3D deconvolution. *Inverse Probl.*, **40(6)**, 065003 (2024).
39. J. L. Schönberger, J.-M. Frahm, Structure-from-Motion Revisited. *IEEE Conference on Computer Vision and Pattern Recognition (CVPR)*, Las Vegas, NV, USA, 12 December 2016.
40. J. L. Schönberger, E. Zheng, J.-M. Frahm, M. Pollefeys, Pixelwise view selection for unstructured multi-view stereo. *In European Conference on Computer Vision (ECCV)*, Amsterdam, The Netherlands, October 11-14, 2016.
41. L. Pan, D. Baráth, M. Pollefeys, J. L. Schönberger, Global structure-from-motion revisited. *In European Conference on Computer Vision (ECCV)*, 58–77, 2025.
42. I. Kurmi, D.C. Schedl, O. Bimber, Airborne Optical Sectioning. *J. Imaging*, **4**, 102 (2018).
43. O. Bimber, I. Kurmi, D. C. Schedl, Synthetic aperture imaging with drones. *IEEE Computer Graphics and Applications*. **39**, 8 – 15 (2019).

44. I. Kurmi, D. C. Schedl, O. Bimber, A statistical view on synthetic aperture imaging for occlusion removal. *IEEE Sensors J.* **19**, 9374 – 9383 (2019).
45. I. Kurmi, D. C. Schedl, O. Bimber, Thermal airborne optical sectioning. *Remote Sens.* **11**, 1668 (2019).
46. D. C. Schedl, I. Kurmi, O. Bimber, Airborne Optical Sectioning for Nesting Observation. *Sci Rep*, **10**, 7254 (2020).
47. I. Kurmi, D. C. Schedl, O. Bimber, Fast automatic visibility optimization for thermal synthetic aperture visualization. *IEEE Geosci. Remote Sens.* **18**, 836-840 (2020).
48. I. Kurmi, D. C. Schedl, O. Bimber, Pose Error Reduction for Focus Enhancement in Thermal Synthetic Aperture Visualization. *IEEE Geosci. Remote Sens.* **19**, 1-5 (2021).
49. D. C. Schedl, I. Kurmi, O. Bimber, Search and rescue with airborne optical sectioning. *Nat. Mach. Intell.*, **2**, 783-790 (2020)
50. D. C. Schedl, I. Kurmi, O. Bimber, An autonomous drone for search and rescue in forests using airborne optical sectioning. *Sci. Robot.*, **6(55)**, 1188 (2021)
51. I. Kurmi, D. C. Schedl, O. Bimber, Combined Person Classification with Airborne Optical Sectioning. *Nature Scientific Reports*, **12**, 3804 (2022)
52. R. J. A. A. Nathan, I. Kurmi, D. C. Schedl, O. Bimber, Through-Foliage Tracking with Airborne Optical Sectioning. *J. Remote Sens.* **2022**, 9812765 (2022)
53. R. J. A. A. Nathan, I. Kurmi, O. Bimber, Inverse Airborne Optical Sectioning. *Drones*, **6**, 9 (2022)
54. F. Seits, I. Kurmi, O. Bimber, Evaluation of Color Anomaly Detection in Multispectral Images For Synthetic Aperture Sensing, *Eng*, **3(4)**, 541-553 (2022)
55. R. J. A. A. Nathan, I. Kurmi, O. Bimber, Drone swarm strategy for the detection and tracking of occluded targets in complex environments. *Commun Eng*, **2**, 55 (2023)
56. R. J. A. A. Nathan, O. Bimber, Synthetic Aperture Anomaly Imaging for Through-Foliage Target Detection. *Remote Sens.*, **15**, 18 (2023)
57. R. Kerschner, R. J. A. A. Nathan, R. Mantiuk, O. Bimber, Stereoscopic Depth Perception Through Foliage. *Nature Scientific Reports*, **14**, 23056 (2024).
58. M. Youssef, O. Bimber, Fusion of Single and Integral Multispectral Aerial Images. *Remote Sens.*, **16(4)**, 673 (2024)
59. R. J. A. A. Nathan, S. Strand, D. Shutin, O. Bimber, Reciprocal Visibility for Guided Occlusion Removal With Drones. *IEEE Geosci. Remote Sens.* **21**, 1 – 5 (2024).
60. Y. Jin, M. Qian, J. Xiong, N. Xue, G.S. Xia, Depth and DOF Cues Make A Better Defocus Blur Detector. In 2023 IEEE International Conference on Multimedia and Expo (ICME), 882-887 (2023).
61. Y.Y. Schechner, N. Kiryati, Depth from Defocus vs. Stereo: How Different Really Are They?. *International Journal of Computer Vision*, **39**, 141–162 (2000).
62. Y. Huihui, L. Daoliang, C. Yingyi, A state-of-the-art review of image motion deblurring techniques in precision agriculture. *Heliyon*, **9**, 6 (2023).
63. C. Zhang, H. Jiang, W. Liu, J. Li, S. Tang, M. Juhas, Y. Zhang, Correction of out-of-focus microscopic images by deep learning. *Computational and Structural Biotechnology Journal*, **20**, 1957 – 1966 (2022).
64. A. K. M. Rabby et al., <https://arxiv.org/pdf/2306.03000> (2023).
65. J. W. Rouse, R. H. Haas, J. A. Schell, D. W. Deering, Monitoring vegetation systems in the Great Plains with ERTS. *NASA Spec. Publ.* **351(1)**, 309 (1974).
66. N. Camarretta, P.A. Harrison, T. Bailey, B. Potts, A. Lucieer, N. Davidson, M. Hunt, Monitoring forest structure to guide adaptive management of forest restoration: a review of remote sensing approaches. *New Forests*, **51(4)**, 573-596 (2020).

67. M. Ehbrecht, D. Seidel, P. Annighöfer, H. Kreft, M. Köhler, D.C. Zemp, K. Puettmann, R. Nilus, F. Babweteera, K. Willim, M. Stiers, Global patterns and climatic controls of forest structural complexity. *Nat. Commun.*, **12**(1), 519 (2021).
68. M.D. Mahecha, A. Bastos, F.J. Bohn, N. Eisenhauer, H. Feilhauer, H. Hartmann, T. Hickler, H. Kalesse-Los, M. Migliavacca, F.E. Otto, J. Peng, Biodiversity loss and climate extremes—study the feedbacks. *Nature*, **612**(7938), 30-32 (2022).
69. A.A. Gitelson, M.N. Merzlyak, Remote Estimation of Chlorophyll Content in Higher Plant Leaves. *Int. J. Remote Sens.*, **18**, 2691–2697 (1997).
70. V. Kopačková-Strnadová, L. Koucká, J. Jelének, Z. Lhotáková, F. Oulehle, Canopy Top, Height and Photosynthetic Pigment Estimation Using Parrot Sequoia Multispectral Imagery and the Unmanned Aerial Vehicle (UAV). *Remote Sens.*, **13**, 705 (2021).
71. J. Villacrés, F. A. Auat Cheein, Construction of 3D maps of vegetation indices retrieved from UAV multispectral imagery in forested areas. *Biosystems Engineering*, **213**, 76 (2022).
72. N. Takhtkeshha, G. Mandlbürger, F. Remondino, J. Hyypä, Multispectral Light Detection and Ranging Technology and Applications: A Review. *Sensors*, **24**, 1669 (2024).
73. S. Vélez, R. Martínez-Peña, D. Castrillo, Beyond Vegetation: A Review Unveiling Additional Insights into Agriculture and Forestry through the Application of Vegetation Indices. *J-Multidisciplinary Scientific Journal*, **6**(3), 421-436 (2023).
74. E. C. Reinisch, A. Ziemann, E. B. Flynn, J. Theiler, Combining multispectral imagery and synthetic aperture radar for detecting deforestation. *In Algorithms, Technologies, and Applications for Multispectral and Hyperspectral Imagery XXVI*, **11392**, 72-85 (2020).
75. A.A. Gitelson, Y.J. Kaufman, R. Stark, D. Rundquist, Novel Algorithms for Remote Estimation of Vegetation Fraction. *Remote Sens. Environ.*, **80**, 76–87 (2002).
76. P. Trybała, L. Morelli, F. Remondino, L. Farrand, M.S. Couceiro, Under-Canopy Drone 3D Surveys for Wild Fruit Hotspot Mapping. *Drones.*, **8**(10), 577 (2024).
77. X. Liang, H. Yao, H. Qi, X. Wang, Forest in situ observations through a fully automated under-canopy unmanned aerial vehicle. *Geo-Spatial Information Science*, **27**(4), 983–999 (2024).
78. R. O. Zanone, T. Liu, J. M. Velni, A Drone-based Prototype Design and Testing for Under-the-canopy Imaging and Onboard Data Analytics. *IFAC-PapersOnLine*, **55**(32), 171-176 (2022).
79. Y. Chen, J. Sun, L. Wang, S. Shi, F. Qiu, W. Gong, T. Tagesson, Exploring the potential of transmittance vegetation indices for leaf functional traits retrieval. *GIScience & Remote Sensing*, **60**(1), (2023).
80. G. Yan, R. Hu, J. Luo, M. Weiss, H. Jiang, X. Mu, D. Xie, W. Zhang, Review of indirect optical measurements of leaf area index: Recent advances, challenges, and perspectives. *Agricultural and Forest Meteorology*, **265**, 390-411 (2019).

Acknowledgments

We thank Rakesh Amala Arokia Nathan of Johannes Kepler University and Dmitri Shutin of the German Aerospace Center for their support during the field experiment, Lukas Bostelmann-Arp, Christoph Steup, and Sanaz Mostaghim of Otto-von-Guericke-University Magdeburg for their contributions to the procedural forest simulator, David Coomes of University of Cambridge and Harald Vacik of BOKU University for fruitful discussions, as well as Ingrid Abfalter for scientific editing and proof-reading.

Funding:

Linz Institute of Technology grant LIT-2022-11-SEE-112 (OB)

Austrian Science Fund (FWF), German Research Foundation (DFG) grant I 6046-N (OB)

Author contributions:

Conceptualization: OB

Methodology: OB, MY

Investigation: OB, MY, JP

Visualization: OB, MY

Supervision: OB

Writing—original draft: OB, MY, JP

Writing—review & editing: OB, MY, JP

Competing interests:

Authors declare that they have no competing interests.

Data and materials availability:

All data are available in the main text or the *Supplementary Materials*. It can be accessed through <https://doi.org/10.5281/zenodo.14748447>

Supplementary Materials for
DeepForest: Sensing Into Self-Occluding Volumes of Vegetation
With Aerial Imaging

Mohamed Youssef, Jian Peng, and Oliver Bimber*

*Corresponding author. Email: oliver.bimber@jku.at

This PDF file includes:

- Figs. S1 to S4
- Movies S1 to S3
- Data S1 to S11
- Code S1 to S2

Other Supplementary Materials for this manuscript include the following:

- Movies S1 to S3
- Data S1 to S11
- Code S1 to S2

Data and materials availability:

All all material below can be accessed through <https://doi.org/10.5281/zenodo.14748447>

Supplementary Material for Reconstruction Error Suppression

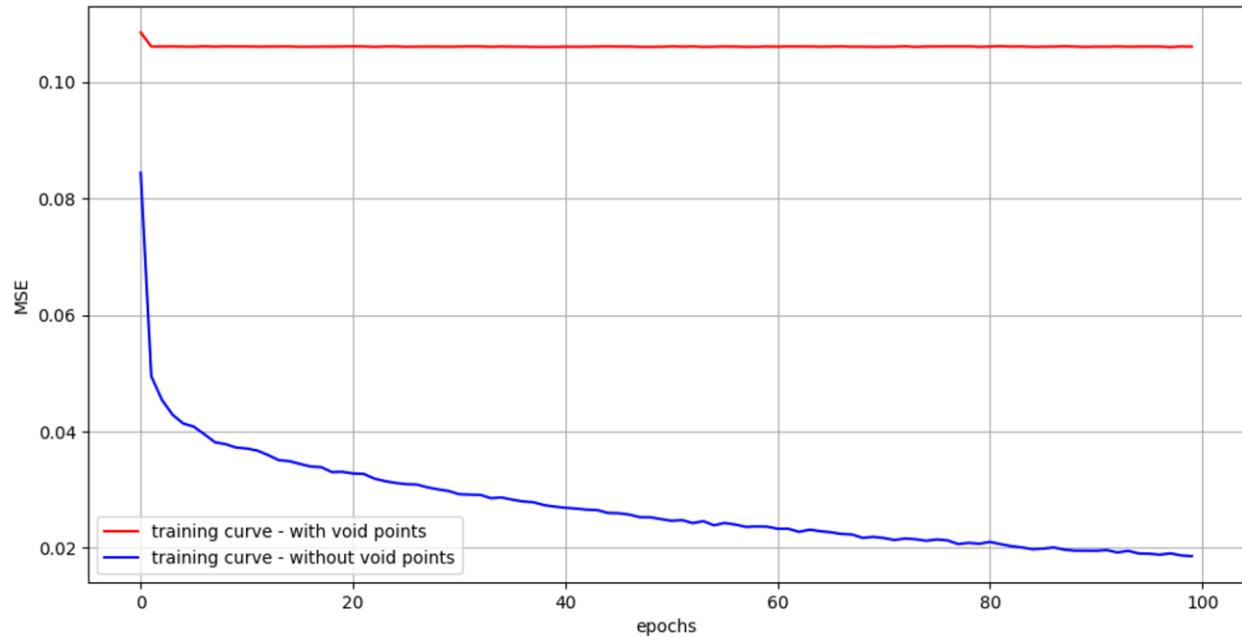


Fig. S1. Training curves for 7m AGL. The plots show that the training of our 3D CNN converges towards a minimal loss only if non-void points are considered (blue). If void points are considered in addition (assuming zero reflectance at these points), training fails (red). Mean-squared-error (MSE) has been used as a loss function, while Adam was applied for optimization. Note that these curves illustrate the training convergence of a deep layer (7m AGL), but the same behaviour can be observed throughout all layers.

Code S1. Python script used for producing the simulation results for training, inference, and testing using the GAZEBO-based drone simulator (https://github.com/bostelma/gazebo_sim).

Code S2. Python code for preprocessing the input and training data, training our models, and final inference (reconstruction). See included readme file for details.

Data S1. Pre-trained models for all 440 layers, as used for producing the results in this article.

Supplementary Material for Simulated Results

Movie S1. Animated version of Fig. 3 (bottom row) and Fig. 6. Raw focal stack, focal stack before and after correction, ground truth forest plot, and photogrammetric reconstruction. Reflectance values are within the same global range (0..1) and color coded. Volumes are visualized with no full opacity to display intrinsic structures.

Data S2. Raw data of simulation. Grid (9x9) of multi-view aerial images (TD_pose_0_rgb.png...TD_pose_80_rgb.png in the images folder) and poses (poses.txt in the poses folder, where the first line is the pose_0 and the last line is pose_80) that were used to compute datasets *Data S1-S4*. In addition, we provide integral images for each focal stack layer (Layer_1.png ...Layer_440.png in the integrals folder) in the and a compilation of all layers in one image stack (integrals.tif).

Data S3. Dataset of original ground truth geometry and reflectance (Fig. 6, first row). The .tif file can be viewed in ParaView (TIFF Series Reader). It contains only one channel (TIFF Scalars) that stores the original simulated reflectance values.

Data S4. Dataset of uncorrected focal stack (Fig. 6, second row). The .vti file can be viewed in ParaView. The different channels contain the following data: uncorrected reflectance values of focal stack (Color, channels_and_opacity, x), ground truth geometry (Color, channels_and_opacity, y), COLMAP geometry reconstruction (Opacity, opacity). For visualization in ParaView, select *color* to be the uncorrected focal stack (Color, channels_and_opacity, x) and *opacity* to be either ground truth geometry (Color, channels_and_opacity, y) or the COLMAP geometry reconstruction (Opacity, opacity). Adapt the transfer function for blending.

Data S5. Dataset of corrected reflectance stack (Fig. 6, third row). The .vti file can be viewed in ParaView. The different channels contain the following data: corrected reflectance values of reflectance stack (Color, channels_and_opacity, x), ground truth geometry (Color, channels_and_opacity, y), COLMAP geometry reconstruction (Opacity, opacity). For visualization in ParaView, select *color* to be the corrected reflectance stack (Color, channels_and_opacity, x) and *opacity* to be either ground truth geometry (Color, channels_and_opacity, y) or the COLMAP geometry reconstruction. Adapt the transfer function for blending.

Data S6. Dataset of original photogrammetry-based (COLMAP) point-cloud reconstruction – including point geometry and reflectance values (Fig. 6, bottom row). The .vtk file can be viewed in ParaView. It contains only one channel (Results) that stores the original reflectance values determined by COMAP.

Supplementary Material for Field Experiment

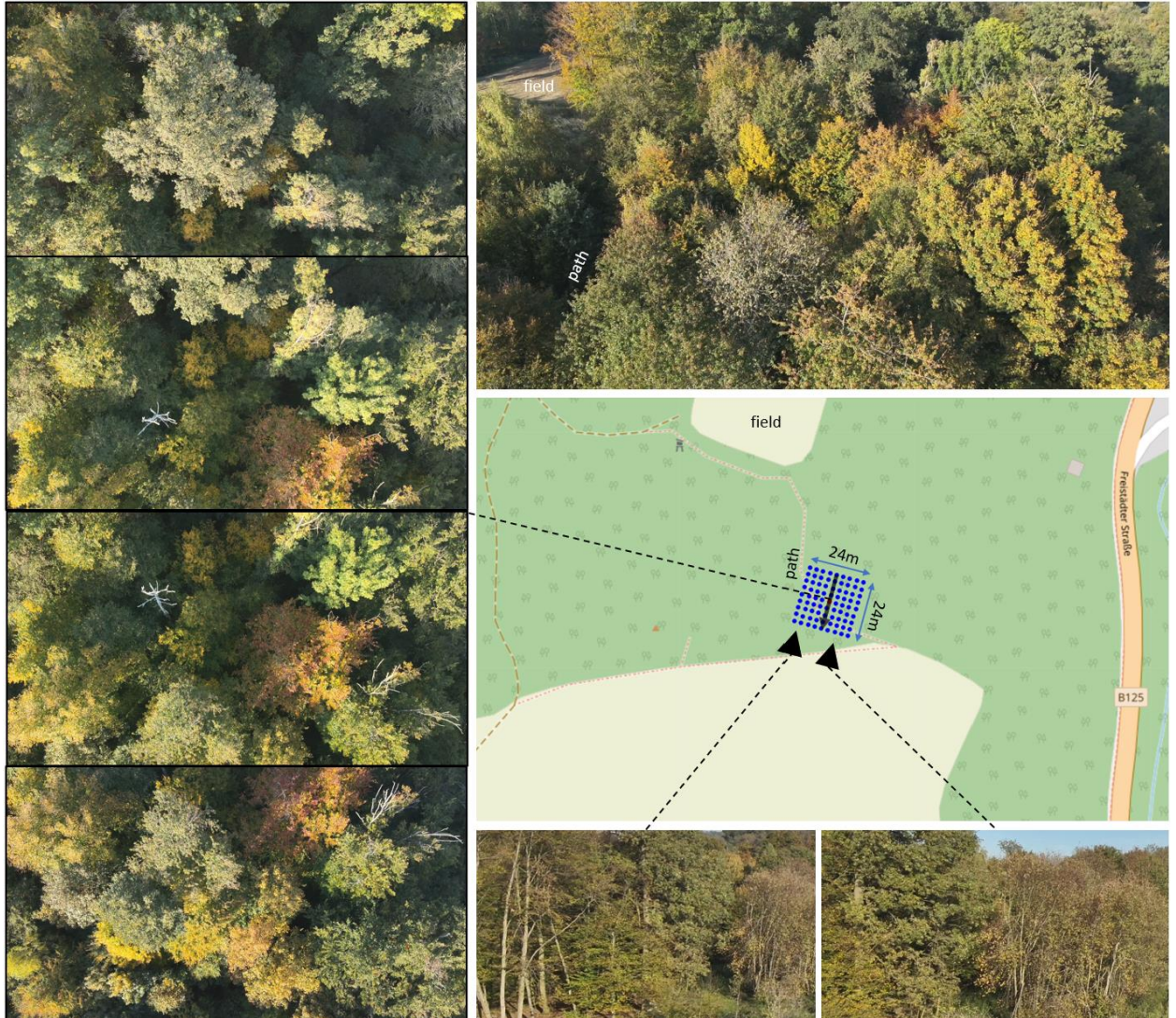


Fig. S2. Forest plot for field experiment. The 24mx24m synthetic aperture and its 9x9 sample poses are illustrated on the map. Various top-down (left), side (bottom), and oblique (top) RGB views of the scanned 30mx30m forest plot are shown. Note, that these images have been taken 3 hours after the scan flight (at around 4pm). The sun is lower in these recordings than during the scan flight at 1pm.



Fig. S3. Drone platform for field experiment. A DJI Matric 30T equipped with an additional Parrot Sequoia+ multispectral camera and sun-light sensor (both powered by the drone’s batteries though DJI’s e-port). Maximum take-off weight is 3.7kg. The drone’s in-built RGB camera was used for flight navigation. Sample images recorded during our field experiment.

Movie S2. Animated version of Fig. 8. Raw multispectral (green=GRE, near-infrared=NIR, red=RED, red-edge=REG, and RGB) focal stacks of field experiment (focussing top-down, from highest tree-crown at 20m AGL to surface of forest). For NIR and RED: uncorrected focal stack, corrected reflectance stack, corrected reflectance stack (sensor-mapped), extracted top vegetation layer (corrected and sensor mapped).

Movie S3. Animated version of Fig. 9. NDVI stack computed from corrected and sensor-mapped RED and NIR reflectance stacks. Extracted top vegetation layer (COLMAP reconstruction) from NDVI stack (two different color maps). Values above the top vegetation layer are removed from NDVI stack. Cropping and range filtering of NDVI stack.

Data S7. Raw data of field experiment. For each spectral channel (see folders: green=GRE, near-infrared=NIR, red=RED, red-edge=REG, and RGB) we provide original aerial images (but cropped to a square resolution, stored as .png in the images folder) and corresponding poses (stored in a .json file in the poses folder). In addition, we provide integral images for each focal stack layer (0.png ...439.png in the integrals folder) and a compilation of all layers in one image stack (integrals.tif). For the RGB channel, we provide the integral images in full resolution but cropped to square (in the integrals_full_resolution folder), and in a downsampled resolution that matches the resolution (440x440px) of the integrals of the other spectral channels (in the integrals_440 folder).

Data S8. Datasets of uncorrected focal stacks, corrected, and corrected + sensor mapped reflectance stacks (Fig. 8). The .vti files can be viewed in ParaView. The different channels contain the following data: reflectance values (Color, channels_and_opacity, x), COLMAP geometry reconstruction from RED or NIR images (Opacity, opacity). For visualization in ParaView, select *color* to be the uncorrected focal stack / the corrected + sensor mapped

reflectance stack (channels_and_opacity, x) and optionally *opacity* to be the COLMAP geometry reconstruction (Opacity, opacity). Adapt the transfer function for blending.

Data S9. Dataset of NDVI stack (computed from corrected and sensor-mapped RED and NIR reflectance stacks, Fig. 9). The .vti files can be viewed in ParaView. The different channels contain the following data: NDVI values (Color, channels_and_opacity, x), COLMAP geometry reconstruction with point-clouds merged from RED and NIR images (Opacity, opacity). For visualization in ParaView, select *color* to be the NDVI stack stack (channels_and_opacity, x) and optionally *opacity* to be the COLMAP geometry reconstruction (Opacity, opacity). Adapt the transfer function for blending.

Data S10. Dataset of NDVI stack as in Data S9, but with values above the top vegetation layer removed. The .vti files can be viewed in ParaView. The different channels contain the following data: NDVI values (Color, channels_and_opacity, x) with values above the top vegetation layer = -1.01, binary mask with 0 values above the top vegetation layer and 1 values below and on the top vegetation layer (Opacity, opacity). For visualization in ParaView, select *color* to be the NDVI stack stack (channels_and_opacity, x) and optionally *opacity* to be the binary mask (Opacity, opacity). Adapt the transfer function for blending (for Color, channels_and_opacity, x values should be > -1.01).

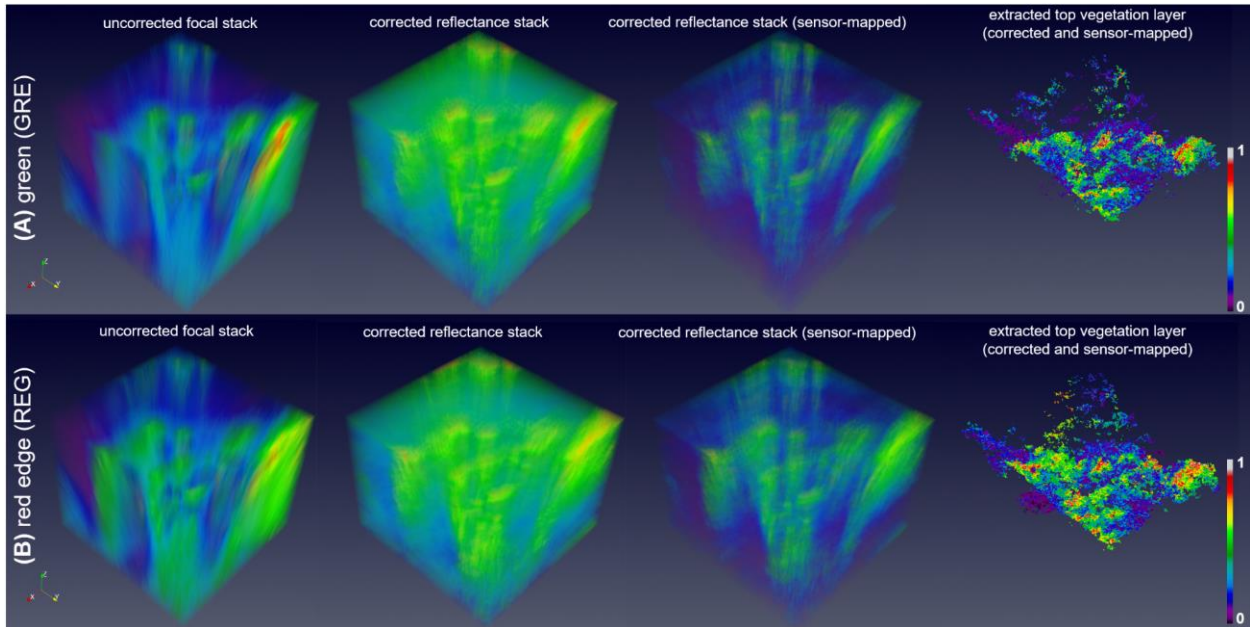


Fig. S4. Red edge (REG) and green (GRE) channels. Uncorrected focal stacks, corrected and sensor-mapped reflectance stacks, and extracted top vegetation layer point clouds of GRE (A) and REG (B) channels. Reflectance values are color coded and within the same global range (0..1). Volumes are visualized with no full opacity to display intrinsic structures. The datasets are provided in *Data S11*. Note, that these datasets were recorded during the field experiments together with RED and NIR, but were not used in the manuscript.

Data S11. Datasets of uncorrected focal stacks, corrected, and corrected + sensor mapped reflectance stacks for green and red edge channels (Fig. S4). The .vti files can be viewed in ParaView. The different channels contain the following data: reflectance values (Color, channels_and_opacity, x), COLMAP geometry reconstruction from REG or GREEN images (Opacity, opacity). For visualization in ParaView, select *color* to be the uncorrected focal stack / the corrected + sensor mapped reflectance stack (channels_and_opacity, x) and optionally *opacity* to be the COLMAP geometry reconstruction (Opacity, opacity). Adapt the transfer function for blending.